Transcriptional Dynamics Uncover the Role of BNIP3 in Mitophagy during Muscle Remodeling in *Drosophila*

(Running title: BNIP3-mediated mitophagy in fly muscle)

Hiroki Taoka[1,3,#], Tadayoshi Murakawa[2,#], Kohei Kawaguchi[1], Michiko Koizumi[1], Tatsuya Kaminishi[4], Yuriko Sakamaki[5], Kaori Tanaka[6], Akihito Harada[6,7], Keiichi Inoue[8], Tomotake Kanki[8], Yasuyuki Ohkawa[6], and Naonobu Fujita[1,2,*]

[1] Cell Biology Center, Institute of Integrated Research, Institute of Science Tokyo, 4259 S2-11 Nagatsuta, Midori-ku, Yokohama, Kanagawa 226-8501, Japan.

[2] School of Life Science and Technology, Institute of Science Tokyo, Yokohama, Kanagawa, Japan.

[3] Biological Science Research Laboratories, Kao Corporation, 2606, Akabane, Ichikai, Haga-gun, Tochigi 321-3497, Japan.

[4] Department of Genetics, Graduate School of Medicine, Osaka University, 2-2 Yamadaoka, Suita, Osaka 565-0871, Japan.

[5] Ochanomizu Research Facility (ORF), Bioscience Center, Research Infrastructure Management Center, Institute of Science Tokyo, 1-5-45, Yushima, Bunkyo-ku, Tokyo 113-8510, Japan.

[6] Division of Transcriptomics, Medical Institute of Bioregulation, Kyushu University, 3-1-1, Maidashi, Higashi-ku, Fukuoka 812-8582, Japan.

[7] Department of Multi-Omics, Graduate School of Medical Sciences, Kyushu University, 3-1-1 Maidashi, Higashi-ku, Fukuoka 812-8582, Japan.

[8] Department of Cellular Physiology, Graduate School of Medical Sciences, Kyushu University, 3-1-1 Maidashi, Higashi-ku, Fukuoka 812-8582, Japan.

[#] These authors equally contributed to this work.

* Corresponding author. Tel: +81 45 924 5131; E-mail: nafujita@cbc.iir.isct.ac.jp

Keywords: Muscle, *Drosophila*, Remodeling, BNIP3, mitochondria, RNA-seq, autophagy

Impact statement: A time-course RNA-seq analysis of muscle remodeling reveals transcriptional dynamics independent of autophagy and highlights the significance of BNIP3 in mitochondrial degradation *in vivo*.

Abbreviations used: APF, after puparium formation; ATG, autophagy-related; DIOM, dorsal internal oblique muscle; GO, gene ontology; LBWM, larval body wall muscle; LIR, LC3/Atg8-interacting regions; MER, minimal essential region; Mito-QC, mitophagy quality control; PCA, principal component analysis; TEM, transmission electron microscopy; TORC1, target of rapamycin complex 1; 3IL, third instar larvae.

Abstract

Differentiated muscle cells contain myofibrils and well-organized organelles, enabling powerful contractions. Muscle cell reorganization occurs in response to various physiological stimuli; however, the mechanisms behind this remodeling remain enigmatic due to the lack of a genetically trackable system. Previously, we reported that a subset of larval muscle cells is remodeled into adult abdominal muscle through an autophagy-dependent mechanism in *Drosophila*. To unveil the underlying mechanisms of this remodeling, we performed a comparative time-course RNA-seq analysis of isolated muscle cells with or without autophagy. It revealed both transcriptional dynamics independent of autophagy and highlighted the significance of BNIP3-mediated mitophagy in muscle remodeling. Mechanistically, we found that BNIP3 recruits autophagic machinery to mitochondria through its LC3-interacting (LIR) motif and minimal essential region (MER), which interact with Atg8a and Atg18a, respectively. Loss of BNIP3 leads to a substantial accumulation of larval mitochondria, ultimately impairing muscle remodeling. In summary, this study demonstrates that BNIP3-dependent mitophagy is critical for orchestrating the dynamic process of muscle remodeling.

Introduction

Differentiated muscle cells are intricate assemblies of myofibrils and well-organized organelles, such as T-tubules and the sarcoplasmic reticulum. Coordinated sliding of actin and myosin filaments is regulated by the dynamics of calcium ions (Ca^{2+}) released from the sarcoplasmic reticulum, while mitochondria provide ATP as the energy source driving this process. Consequently, the structural alignment of organelles and myofibrils within muscle cells is essential for the precise orchestration of contraction (Kawaguchi and Fujita, 2024). Muscle cells are long-lived and continuously undergo atrophy and hypertrophy cycles in response to growth factors, mechanical loading, nutrient status, and aging (Sartori et al., 2021). Muscle organelles also undergo remodeling as the amount of myofibrils changes, a process mediated by the ubiquitin-proteasome system. However, the mechanisms behind these processes are still poorly understood due to the lack of a genetically tractable system for analyzing muscle remodeling.

Macroautophagy, hereafter referred to as autophagy, is essential for muscle function in both flies and mammals. Autophagy is an intracellular degradation system that delivers cytosolic materials to the lysosome (Morishita and Mizushima, 2019; Nakatogawa, 2020). A flat membrane sac elongates and encloses cytosolic content to form an autophagosome, a double membrane structure. The completed autophagosome fuse with lysosomes to degrade the enclosed cargo. To date, over 40 *ATG* genes have been identified as key regulators of autophagosome formation and cargo selectivity (Nakatogawa, 2020). In mammalian muscles, the loss of autophagy leads to reduced contractile function and abnormalities in myofibrils and organelles, including mitochondria and sarcoplasmic reticulum (Karsli-Uzunbas et al., 2014; Masiero et al., 2009; Yoshii et al., 2016). We have previously reported that a subset of larval body wall muscle cells is remodeled into adult dorsal internal oblique muscles (DIOM) through an autophagy-mediated mechanism (Fujita et al., 2017; Murakawa et al., 2020). The remodeled adult DIOMs function during eclosion, persist for approximately 12 hours, and are subsequently eliminated via programmed cell death (Kimura and Truman, 1990). To our knowledge, DIOM remodeling is the sole example of developmentally regulated muscle remodeling, making it an ideal model for studying muscle remodeling in general. Autophagy blockade results in severe phenotypes in DIOM (Fujita et al., 2017; Murakawa et al., 2020), yet the mechanisms by which autophagy loss induces defects remain unclear. Given that autophagy contributes to nutrient supply and transcriptional regulation (Morishita and Mizushima, 2019; Sánchez-Martín et al.,

88 2019),it is plausible that dysfunction in autophagy could also impact gene expression during
89 DIOM remodeling.
90 Autophagy can selectively target various substrates, including protein aggregates,
91 invading bacteria into the cytosol, and organelles (Lamark and Johansen, 2021; Vargas et al.,
92 2023). This selectivity is achieved through soluble and transmembrane cargo receptors, which
93 bridge the cargo and autophagy machinery. Most soluble cargo receptors target ubiquitinated
94 cargoes and harbor oligomerization domains, ubiquitin-binding domains, and LC3/Atg8-
95 interacting regions (LIR), which is a four-residue motif [W/F/Y] -X-X-[L/V/I] (Johansen and
96 Lamark, 2020). In contrast, transmembrane cargo receptors are anchored to target organelles
97 and recruit autophagy machinery. Soluble and transmembrane cargo receptors confer selectivity
98 through direct interaction with the ATG machinery. In most cases, in addition to the affinity
99 with Atg8/LC3 via the LIR motif, interaction with core machinery components, such as ULK1,
100 FIP200/Atg11, and Atg9, is required (Lamark and Johansen, 2021).
101 Mitophagy, selective autophagy for mitochondria, is physiologically crucial because
102 mitochondrial malfunction is harmful, resulting in energy insufficiency or excess reactive
103 oxygen species (ROS) in cells (Ney, 2015). In addition to damaged mitochondria, functional
104 mitochondria can be removed by mitophagy to meet distinct cellular demands. Multiple
105 mechanisms exist for mitophagy, including both soluble and transmembrane receptor-mediated
106 mechanisms (Onishi et al., 2021). In soluble receptor-mediated mitophagy, the PINK1/Parkin
107 axis labels mitochondria with ubiquitin. The ubiquitinated mitochondria are then recognized by
108 NDP52 and Optineurin, soluble cargo receptors, leading to their sequestration by autophagic
109 membranes (Narendra and Youle, 2024). On the other hand, transmembrane cargo receptors are
110 anchored to the outer mitochondrial membrane and recruit autophagy machinery via LIR and
111 other motifs interacting with the ATG machinery (Onishi et al., 2021). The concept of receptor-
112 mediated mitophagy was first established in yeast ATG32 studies (Kanki et al., 2009; Okamoto
113 et al., 2009), and then subsequently it was found that the basic mechanisms are also conserved
114 in multicellular organisms. The list of mitochondrial outer membrane-embedded cargo receptors
115 is growing: NIX/BNIP3L, BNIP3, FKBP8, FUNDC1, and BCL2L13 (Onishi et al., 2021).
116 Nevertheless, their relative contribution and molecular mechanisms still need to be fully
117 elucidated, especially under physiological conditions. So far, most mitophagy studies have been

118 performed in cultured cells with uncouplers, hypoxia, or genetic perturbations (Yamashita et al.,
119 2024).
120 NIX (also known as BNIP3L) and BNIP3 are homologous receptors for mitophagy in
121 mammals. NIX was initially discovered as a mitophagy receptor during reticulocyte maturation.
122 Seminal studies discovered that NIX is required to clear mitochondria from reticulocytes during
123 differentiation (Sandoval et al., 2008; Schweers et al., 2007). Following this, its paralog BNIP3
124 was also shown to regulate mitophagy. NIX and BNIP3 have an LIR motif near their N-
125 terminus and a transmembrane domain (TMD) for localization to the mitochondrial outer
126 membrane near their C-terminus. Thereby, it has been proposed that NIX and BINP3 tether the
127 Atg8/LC3-positive isolation membrane and mitochondria for mitophagy through these domains
128 (Li et al., 2022; Onishi et al., 2021; Schwarten et al., 2009). In addition, Prof. Ney's group in the
129 US identified a minimal essential region (MER), a short motif in NIX required for mitochondria
130 clearance in reticulocytes (Zhang et al., 2012). Recently, it has been reported that the MER
131 directly interacts with WIPIs, mammalian Atg18 orthologs, to recruit core autophagy machinery
132 in cultured cells overexpressing BNIP3 (Adriaenssens et al., 2024; Bunker et al., 2023). Despite
133 these findings, the roles of LIR-Atg8 and MER-Atg18 interactions in BNIP3-mediated
134 mitophagy have not been investigated under physiological conditions.
135 *Drosophila* BNIP3, the sole ortholog of NIX and BNIP3, contains LIR, MER, and
136 TMD, similar to its mammalian counterparts. In *Drosophila*, it has been reported that BNIP3
137 plays a role in programmed germline mitophagy required for mitochondrial DNA quality
138 control (Lieber et al., 2019; Palozzi et al., 2022). However, the mechanism is not well
139 understood. In addition, the contribution of BNIP3 to mitophagy in other physiological contexts,
140 such as cellular differentiation or remodeling programs, has not been explored yet. In this study,
141 we performed a comparative time-course RNA-seq analysis of isolated muscle cells, and
142 identified BNIP3-mediated mitophagy as a critical factor in developmentally programmed
143 muscle remodeling. We also explored the underlying mechanism by which BNIP3 tethers
144 mitochondria with the autophagic machinery, as well as the physiological significance of
145 BNIP3-mediated mitophagy *in vivo*.
146

147 **Results**

148 **Transcriptional dynamics of DIOM remodeling during metamorphosis**

149 During DIOM remodeling, autophagy occurs during atrophy, which lasts from 12 h to 2 d APF
150 (after puparium formation). Then, organelle and myofibril reformation accompanies
151 hypertrophy from 2 to 4 d APF (Fig. 1A). We previously reported the dynamics of several
152 organelles in DIOM remodeling (Fujita et al., 2017; Murakawa et al., 2020); however, the
153 overall mechanism is still enigmatic. To gain molecular insights into DIOM remodeling, we
154 performed time-course RNA-seq of isolated DIOMs from four animals at five time points (Fig.
155 1A). Dissected animals were fixed with methanol to avoid cell death induction (Wang et al.,
156 2021), and six DIOMs were isolated from each animal to prep total RNA (Fig. 1B). The
157 mRNAs were amplified, and the cDNA libraries were prepared using CEL-Seq2, a sensitive
158 protocol for single-cell RNA-seq (Hashimshony et al., 2016). Then, they are subjected to next-
159 generation sequencing. As a result, ~8,000 genes were counted in the DIOMs above background
160 (Supplementary File 1, ctrl). High similarities among four replicates at each time point show the
161 reproducibility of our protocol (Fig. 1-figure supplement 1A). We performed DESeq2 principal
162 component analysis (PCA) of all samples to reduce the dimensionality of the data (Fig. 1C and
163 Fig. 1-figure supplement 1B). In the PC1-PC2 plane, which explains 43% of expressed genes in
164 DIOMs, the transcriptome changed dynamically from 3IL to 4 d APF (Fig. 1C). Of note, there
165 was a substantial difference between before (3IL) and after (4 d APF) remodeling in both PC1-2
166 and PC3-4 (Fig. 1C), suggesting the functional importance of remodeling larval muscle to adult
167 abdominal muscle during this epoch.

168 To identify genes with similar temporal expression profiles, we used Fuzzy c-means to
169 categorize normalized read counts into twelve clusters (Fig. 1-figure supplement 1C), each with
170 379 to 937 genes (Fig. 1-figure supplement 1D). The twelve clusters represent unique temporal
171 expression dynamics, with each time point showing a distinct profile of clusters with high
172 expression (Fig. 1D and Fig. 1-figure supplement 1D). We also noticed that a time-dependent
173 shift in gene ontology (GO) terms is apparent among the clusters, reflecting the sequential
174 events during DIOM remodeling (Fig. 1F). The principal component coefficients (loadings) of
175 individual clusters to PC1 through 4 are shown in Fig. 1E. The direction and length of the
176 arrows indicate the contribution of each cluster to principal components (PC1 to 4). Briefly,
177 upon induction of muscle atrophy (1-2 d APF), the ubiquitin-proteasome system, developmental

178 signaling, autophagy, and histone modifications-related genes were upregulated. Then,
179 chromatin remodeling-related genes were elevated around 2 d APF. Myofibril, mitochondrion,
180 and ribosome biogenesis-related genes required for muscle hypertrophy were upregulated
181 around 3 d APF (Fig. 1F). The data illustrates the sequential events involved in DIOM
182 remodeling, aligning with previously observed morphological changes (Fujita et al., 2017;
183 Murakawa et al., 2020).
184
185 **Transcriptional dynamics occur independently of autophagy during DIOM remodeling**
186 Autophagy deficiency impacts both atrophy and myofibril regeneration during hypertrophy
187 (Fujita et al., 2017; Murakawa et al., 2020) (Fig. 2A). Given that autophagy is known to
188 influence gene expression through both direct and indirect mechanisms (Morishita and
189 Mizushima, 2019; Sánchez-Martín et al., 2019), we hypothesized that the loss of autophagy also
190 alters gene expression in DIOMs. To investigate this possibility, we performed a comparative
191 time-course RNA-seq of DIOM remodeling in *Atg18a* RNAi, *FIP200* RNAi, or *Stx17* RNAi
192 DIOMs and compared the results with control data (Fig. 2B). Atg18a and FIP200 are essential
193 factors for autophagosome formation, and Stx17 is an autophagosomal SNARE protein required
194 for autophagosome-lysosome fusion (Lőrincz and Juhász, 2020; Nakatogawa, 2020). Thus, their
195 knockdown blocks autophagy at early or late stages, respectively (Fig. 2B, bottom). Similar to
196 the experiment in Fig. 1, we performed RNA-seq at five time points from 3IL to 4 d APF (Fig.
197 2B) and confirmed high similarities among the four replicates in all 20 conditions (Fig. 2-figure
198 supplement 1A and Supplementary File 1). We confirmed that RNAi efficiently knocked down
199 targeted genes (Fig. 2-figure supplement 1B-D). In contrast to our prediction, the knockdown of
200 *Atg18a*, *FIP200*, or *Stx17* only had a slight impact on transcriptomic dynamics in DIOM
201 remodeling (Fig. 2C), with only minor changes detected (Fig. 2-figure supplement 2G).
202 Next, to examine whether loss of autophagy affects protein synthesis in DIOMs, we
203 used the quantification of DIOM volume changes as a surrogate measurement, and compared
204 controls with *FIP200* RNAi from 3IL to 4 d APF (Fig. 2D and E). As expected, muscle atrophy
205 observed until 2 d APF was affected by *FIP200* RNAi (Fig. 2A and D). Notably, DIOMs in the
206 *FIP200* RNAi condition grew from 2 to 3 d APF at levels comparable to the control (Fig. 2E),
207 indicating that protein synthesis occurs independently of autophagy. Consistent with this
208 observation, transcription of both ribosomal RNAs and proteins, established indicators of the

209 target of rapamycin complex 1 (TORC1) activity (Saxton and Sabatini, 2017), did not drop but
210 instead were slightly elevated in conditions lacking autophagy (Fig. 2-figure supplement 2). The
211 synthesis of rRNA was upregulated in *ATG* RNAi between 2 to 3 d APF (Fig. 2-figure
212 supplement 2A). It was confirmed that the number of nuclei remained unchanged by the loss of
213 autophagy (Fig. 2-figure supplement 2B-C). The size of the nucleolus, which positively
214 correlates with TORC1 activity (Grewal et al., 2007), was increased by *FIP200* and *Stx17* RNAi
215 (Fig. 2-figure supplement 2D-F). Moreover, most ribosomal protein large subunit (RpLs) and
216 ribosomal protein small subunit (RpSs) mRNA levels were higher in *ATG* RNAi conditions
217 (Fig. 2-figure supplement 2G). These results suggest that TORC1 activity and protein synthesis
218 capacity are comparable between control and autophagy-deficient DIOMs. Altogether, we
219 conclude that gene expression occurs independently of autophagy in DIOMs.
220
221 **Loss of BNIP3 leads to an accumulation of mitochondria in DIOMs**
222 The above results suggest that the autophagic degradation of cytosolic components in itself is
223 critical for DIOM remodeling. We have previously reported that *FIP200* RNAi or *Stx17* RNAi
224 induce the accumulation of mitochondria or mitophagosomes, respectively (Fig. 3A and B)
225 (Fujita et al., 2017). In addition, mitophagosomes were often observed in wild-type DIOMs at 1
226 d APF, when autophagy is strongly induced (Fig. 3C) (Fujita et al., 2017). These results suggest
227 that mitochondria are major autophagy cargo, and impaired mitophagy contributes to the severe
228 loss of autophagy phenotype.
229 We tried to identify relevant mitophagy receptors directly via our RNA-seq approach.
230 The time course RNA-seq data (Fig. 1 and 2) indicated that *BNIP3* was robustly expressed in 1
231 d APF DIOMs among known mitophagy regulators (Fig. 3D). *Zonda*, *CG12511*, *Key*, and
232 *Ref(2)P* are *Drosophila* orthologs of FKBP8, FUNDC1, Optineurin, and p62, respectively.
233 BNIP3 is the sole fly ortholog of mammalian NIX and BNIP3. *BNIP3* mRNA levels were
234 relatively high at 3IL and 4 d APF when mitophagy was minimally induced. We noticed that
235 *FBXL4* is expressed in 3IL and 4 d APF but not in 1 d APF DIOM (Fig. 3E). BNIP3 is known to
236 undergo ubiquitination and degradation through a mechanism mediated by FBXL4, a ubiquitin
237 E3 ligase (Niemi and Friedman, 2024). Previous data suggest that transcriptional and post-
238 translational mechanisms regulate BNIP3 protein levels. Consistent with expression levels,
239 *BNIP3* RNAi led to mitochondrial accumulation in 4 d APF DIOMs, whereas RNAi targeting

240 other known mitophagy regulators did not (Fig. 3-figure supplement 1). We generated *BNIP3*
241 knockout (KO) flies lacking all exons using two gRNA to characterize BNIP3 further (Fig. 3F).
242 *BNIP3* KO was compatible with viability and did not markedly impair mobility (Fig. 3-figure
243 supplement 2A-C). Similar to RNAi, mitochondria accumulated significantly in *BNIP3* KO
244 DIOMs at 4 d APF (Fig. 3G).
245 At the ultrastructural level, *BNIP3* KO induced the accumulation of mitochondria and
246 loss of myofibrils (Fig. 4A-C), consistent with our confocal data (Fig. 3G). To test the role of
247 BNIP3 in mitophagosome formation more directly, we performed TEM in the absence of Stx17
248 to block the autophagosome-lysosome fusion. As expected, mitophagosomes (pink-colored)
249 were frequently observed in the *Stx17* RNAi condition (Fig. 4D, D' and F). In stark contrast,
250 mitophagosomes were rare, and unengulfed mitochondria (green-colored) accumulated in the
251 combined condition of *Stx17* RNAi and *BNIP3* KO (Fig. 4E, E', and F). We also confirmed
252 there was no significant difference in the number of autophagosomes (blue-colored) between the
253 two conditions (Fig. 4G), indicating that BNIP3 is dispensable for autophagosome formation.
254 These data show that BNIP3 is critical for mitophagosome formation in DIOMs.
255
256 **The LIR and MER motifs in BNIP3 are required for the clearance of mitochondria in**
257 **DIOMs**
258 *Drosophila* BNIP3 harbors LIR, MER, and TMD domains, similar to mammalian NIX and
259 BNIP3 (Fig. 5A). Although the function of the MER domain has been unknown since it was
260 identified (Zhang et al., 2012), recent studies have shown that the MER of mammalian NIX and
261 BNIP3 directly interacts with WIPIs, the mammalian orthologs of Atg18 (Adriaenssens et al.,
262 2024; Bunker et al., 2023). AlphaFold 3 (Abramson et al., 2024) predicted that this interaction
263 is evolutionarily conserved in *Drosophila* in a manner analogous to their mammalian
264 counterparts (Fig. 5B) (Adriaenssens et al., 2024; Bunker et al., 2023). In this prediction,
265 residues 31–57 of *Drosophila* BNIP3 (slate blue and yellow) interact with the surface formed by
266 blades 2 (green) and 3 (pink) of the β-propeller structure of *Drosophila* Atg18a. Notably,
267 residues 42–53 (yellow), which correspond to the MER designated for NIX (Bunker et al.,
268 2023; Zhang et al., 2012), fold into an α-helix, docking into the groove formed by blades 2 and
269 3 and forming substantial hydrophobic interactions as well as defined polar contacts. We
270 confirmed that HA-tagged *Drosophila* Atg18a co-immunoprecipitated with GFP-tagged full-

271 length *Drosophila* BNIP3, and that this interaction was attenuated by the deletion of the MER
272 (residues 42-53) (Fig. 5C).
273 Next, to verify the importance of the LIR and MER motifs in BNIP3, we expressed a
274 series of BNIP3 mutants in *BNIP3* KO flies (Fig. 5A). ΔLIR (W16A/L19A) lacks critical
275 consensus residues in LIR due to double mutations (Johansen and Lamark, 2020). The MER
276 mutant (MER^{mut}, L49A) substituted residue L49 with an A, which is predicted to be deeply
277 buried at the interface with Atg18a (Fig. 5C). The corresponding L75A mutant in human NIX
278 has been shown to lose its affinity for WIPI2/Atg18 (Bunker et al., 2023). The ΔMER mutant
279 lacks an entire short α-helix (G42 to Q53) of the MER motif (Fig. 5C, shown yellow-orange).
280 The ΔLIR+ΔMER is a combined construct of ΔLIR and ΔMER. All BNIP3 constructs retain an
281 intact TMD at the C-terminus, ensuring their localization to the outer mitochondrial membrane
282 (Fig. 5-figure supplement 1A).
283 As shown in Fig. 5D, the expression of the full-length (Full) construct almost
284 completely suppressed the accumulation of mitochondria in BNIP3 KO at 4 d APF, confirming
285 the rescue of BNIP3 function using our construct-based approach. To our surprise, the BNIP3
286 ΔLIR construct rescued the *BNIP3* KO phenotype comparable to Full, indicating LIR on its own
287 may be redundant for mitophagy in DIOMs. In contrast, mitochondria accumulated in MER^{mut}
288 and ΔMER reconstituted DIOMs. Furthermore, the combination of ΔLIR and ΔMER resulted in
289 mitochondria accumulation nearly identical to that observed in BNIP3 KO flies (Fig. 5D and
290 D'). Consistent with these findings, *Atg101*-dependent autophagic degradation of GFP-BNIP3
291 was strongly suppressed by the ΔLIR+ΔMER mutations (Fig. 5E). Atg101 is an essential
292 subunit of the Atg1/ULK1 kinase complex (Guo et al., 2019; Hegedus et al., 2014; Noda and
293 Mizushima, 2016). From these results, we conclude that both MER and LIR motifs contribute to
294 BNIP3-mediated mitophagy, with some redundancy in their contributions to selectivity.
295
296 **BNIP3-mediated mitophagy eliminates larval muscle mitochondria during muscle**
297 **remodeling**
298 The data above suggest that a BNIP3-mediated mechanism degrades larval muscle-derived
299 mitochondria; however, in previous figures, we only observed the terminal phenotype of *BNIP3*
300 KO at 4 d APF. To observe the changes in the number of mitochondria and cell shape during
301 DIOM remodeling, we first performed a time-course experiment in control and *BNIP3* KO

302 conditions (Fig. 6A and Fig. 6-figure supplement 1A and B). There was no significant
303 difference in the number of mitochondria at 3IL; however, mitochondria started accumulating at
304 1 d APF (Fig. 6A and A'), suggesting that BNIP3-mediated mitophagy degrades larval muscle
305 mitochondria. Further, we tested the Mito-QC probe (Lee et al., 2018), a tandem GFP-mCherry
306 fusion protein targeted to the OMM, to compare mitophagy flux at 1d APF with and without
307 BNIP3. When the probe is delivered to lysosomes via autophagy, the GFP is quenched due to
308 the acidic environment of the lysosome. Robust mitophagy activity was detected in control
309 DIOMs at 1 d APF. In sharp contrast, *BNIP3* KO blocked mitophagy flux at a comparable level
310 with *FIP200* RNAi (Fig. 6B and B').
311 To show the degradation of larval muscle-derived mitochondria more directly, we
312 labeled larval muscle mitochondria specifically by using the temperature-sensitive mutant of
313 GAL80 ($GAL80^{ts}$), a repressor of GAL4 (Mcguire et al., 2004). At the restrictive temperature
314 (29˚C), the $GAL80^{ts}$ mutant is inactive, allowing GAL4 to drive the expression of the UAS-
315 fused construct, UAS-Mito-GFP. Conversely, at the permissive temperature (18˚C), the
316 $GAL80^{ts}$ is active, suppressing GAL4 activity. Using this system, Mito-GFP was expressed in
317 the larval muscle and subsequently suppressed throughout the entire pupal stage (Fig. 6C). Anti-
318 ATP5A antibodies were used to visualize total mitochondria. The amount of Mito-GFP-positive
319 mitochondria was comparable in control and *BNIP3* KO at 3IL muscle. However, at 4 d APF,
320 the Mito-GFP signal was nearly absent in the control, while a strong Mito-GFP signal was
321 observed in the *BNIP3* KO (Fig. 6D and D'), indicating that BNIP3-mediated mitophagy
322 degrades larval muscle mitochondria during muscle remodeling.
323

Discussion

The transcriptional dynamics associated with DIOM remodeling are largely independent of autophagy (Fig.2). Instead, our RNA-seq data suggest that it is regulated primarily by ecdysone signaling, with minimal influence from autophagy inhibition. However, a subset of genes exhibited altered expression levels in autophagy-deficient conditions (Fig. 2-figure supplement 2G). Of note, their expression levels were consistently upregulated or downregulated throughout all time points. Since no apparent phenotype was observed in *ATG* knockdown 3IL body wall muscles (Fujita et al., 2017), the observed expression changes are unlikely to underlie the loss-of-autophagy phenotype in DIOM remodeling. Furthermore, *FIP200* RNAi had minimal impact on the DIOM growth rate (Fig. 2 D and E), which reflects translational capacity. From these data, we conclude that the contribution of autophagy to gene expression during DIOM remodeling is minimal.

In the RNA-seq experiments (Fig. 2), *ATG* genes were exclusively depleted in muscle cells; thus, autophagy in non-muscle organs remained intact. It is plausible that essential nutrients for DIOM hypertrophy, such as amino acids, were supplied by other organs, including the fat body (Murakawa et al., 2022). Alternatively, the necessary amino acids might have been derived from myofibril breakdown via the ubiquitin-proteasome system (Quy et al., 2013).

Transcriptome changes before and after DIOM remodeling reflect adaptations to the shift from the anaerobic environment of larvae to the aerobic environment of adults, alongside alterations in nutritional pathways. Notable changes in energy production systems occurred between the 3IL stage (pre-remodeling) and 4 d APF (post-remodeling) (Fig. 1). Glycolysis-associated genes exhibited high expression levels at the 3IL stage, followed by a significant decline during the pupal and adult stages. For instance, the expression of *Lactate dehydrogenase* (*Ldh*), a key enzyme in switching between anaerobic and aerobic respiration (Liang et al., 2023; Semenza, 2014), was particularly noteworthy. Ldh catalyzes the conversion of pyruvate to lactate while regenerating NAD^+ from NADH under anaerobic conditions. Ldh levels were markedly high in larval muscles, suggesting reliance on anaerobic glycolysis. Conversely, its reduced expression in remodeled adult muscles reflects a metabolic shift toward aerobic pathways.

Genes related to serine-centered amino acid and lipid catabolism, both of which rely on oxygen to produce ATP, were significantly upregulated in adult muscles. For example, the

355 expression of *Alanine-glyoxylate aminotransferase* (*Agxt*), an enzyme that converts alanine to
356 pyruvate, was approximately 100 times higher in adult muscles compared to larvae. Similarly,
357 *brummer* (*bmm*), a triacylglycerol lipase, exhibited a fivefold increase, suggesting enhanced
358 reliance on fatty acids metabolized via β-oxidation and the TCA cycle. These findings highlight
359 the shift in energy sources from glycolysis in larval muscles to amino acids and lipids in adult
360 muscles, metabolized aerobically in mitochondria.

361 A recent study suggests that DIOMs are a primary source of pupal ecdysone (Zhang et
362 al., 2024). In line with this data, our time-course mRNA-seq analysis revealed high expression
363 of *Phm*, an enzyme essential for ecdysteroid biosynthesis, at 1 d APF (Supplementary File 1).
364 However, other Halloween genes required for ecdysteroid biosynthesis, such as *Nvd*, *Spo*, *Spok*,
365 *Dib*, *Sad*, and *Shd* (Kamiyama and Niwa, 2022), were not, or only minimally, expressed in
366 DIOMs during metamorphosis (Supplementary File 1). Consequently, whether DIOMs directly
367 secrete ecdysone remains unclear. Instead, DIOMs may contribute to a specific step in the
368 ecdysteroid biosynthesis pathway, potentially supplying intermediate 5β-ketotriol to other
369 tissues for further conversion.

370 Functional mitochondria are degraded during developmental muscle remodeling;
371 therefore, it is reasonable that a membrane-anchored mitophagy receptor, directly interacting
372 with the autophagic machinery, is selected over a ubiquitination-mediated mechanism involving
373 PINK1 and Parkin. The PINK1/Parkin axis is activated by mitochondrial membrane potential
374 depolarization (Narendra and Youle, 2024), which is not observed in remodeling muscles. The
375 protein level of BNIP3 appears to be regulated at transcriptional and post-translational levels
376 (Fig. 3E). It is known that BNIP3 is degraded via a mechanism mediated by Fbxl4, a ubiquitin
377 E3 ligase (Niemi and Friedman, 2024). The balance between synthesis and degradation likely
378 results in the highest BNIP3 protein levels at 1 d APF, a time when mitophagy is robustly
379 induced. However, BNIP3 protein levels have not been directly confirmed, as isolating a
380 sufficient number of DIOMs for western blotting is challenging. Generating a GFP knock-in
381 line for BNIP3 would allow for an imaging-based assay to measure its protein levels during
382 DIOM remodeling.

383 Overexpression of BNIP3 in larval muscle cells did not significantly induce mitophagy
384 (Fig. 5-figure supplement 2), suggesting that BNIP3 expression alone is insufficient to drive
385 mitophagy. BNIP3-mediated mitophagy likely requires not only BNIP3 expression but also

386 autophagy induction. We propose that autophagy induction in DIOMs at the early pupal stage is
387 regulated by ecdysone signaling, similar to other instances of developmental autophagy in
388 *Drosophila* (Murakawa et al., 2022). Understanding the mechanisms by which developmental
389 signals trigger autophagy remains a critical question for future research.

390 A key function of autophagy in DIOM remodeling is the degradation of mitochondria
391 from larval muscles. In the absence of BNIP3, mitochondria derived from the larval muscle
392 accumulate and cluster in the cell center, physically obstructing myofibril formation during
393 hypertrophy and restricting myofibrils to the cell periphery (Fig. 6E). Interestingly, unlike *ATG*
394 RNAi, *BNIP3* knockout muscles exhibited relatively normal but thinner myofibrils (Fig. 3G). In
395 contrast, *ATG* RNAi not only caused mitochondrial accumulation but also severely disrupted
396 myofibril organization, as indicated by misaligned sarcomeres (Fujita et al., 2017; Murakawa et
397 al., 2020). These findings suggest that autophagy contributes to DIOM remodeling beyond
398 mitochondrial degradation. Schnorrer's group in France has demonstrated that mechanical
399 tension is essential for sarcomere assembly and maturation (Mao et al., 2022; X. Zhang et al.,
400 2024). Given that *ATG* RNAi disrupts DIOM attachment (Murakawa et al., 2020; Ribeiro et al.,
401 2011), it is possible that reduced tension—caused by an unknown mechanism—leads to
402 disorganization of myofibrils in DIOMs when autophagy is impaired.

403 Contrary to the previous model, the LIR motif of BNIP3 was found to be dispensable
404 for mitophagy in DIOMs (Fig. 5D and E). Our findings align with reports stating that the
405 clearance of mitochondria in reticulocytes is independent of the LIR motif (Novak et al., 2010;
406 Zhang et al., 2012). Together, this suggests that the dependency on the LIR motif may differ
407 between *in vitro* and *in vivo* contexts. In studies of BNIP3 in cultured cells, such as HeLa cells,
408 BNIP3 is often overexpressed, and mitophagy is induced through chemical treatments (Bunker
409 et al., 2023; Yamashita et al., 2024). These experimental conditions may account for the
410 observed differences in LIR dependency. Understanding the factors that drive these contextual
411 variations in BNIP3-mediated mitophagy will require further investigation.

412 The MER motif in BNIP3 is required for mitophagy in *Drosophila*. Similar to its
413 mammalian counterpart, the MER motif of *Drosophila* BNIP3 is predicted to interact with the
414 groove between blades 2 and 3 of the β-propeller in Atg18a (Fig. 5B). Notably, this groove of
415 Atg18 overlaps with the binding site for Atg16 (Strong et al., 2021). We propose that the BNIP3
416 MER-Atg18a interaction functions at the early stages of mitophagosome formation, which is

417 later replaced by the Atg16-Atg18a interaction during the elongation phase. In this sequential
418 model, the BNIP3 LIR-Atg8a interaction would dominate at the elongation steps. Alternatively,
419 the MER-Atg18a and LIR-Atg8a interactions might serve redundant roles in determining
420 selectivity, as both Atg8 and Atg18 localize to the elongating autophagic membranes. This
421 redundancy could explain why the LIR motif is dispensable for BNIP3-mediated mitophagy
422 (Fig. 5D and E).
423 Martens's group (Austria) recently reported that WIPIs, the mammalian orthologs of
424 Atg18, bind to Atg13, a component of the FIP200/ULK1 complex (Adriaenssens et al., 2024).
425 They propose that the NIX/BNIP3-WIPI-Atg13 axis induces selective autophagy for
426 mitochondria, analogous to known selective autophagy receptors associated with FIP200
427 (Lamark and Johansen, 2021). It would be interesting to test whether an artificial interaction
428 motif with the Atg1 complex could compensate for the loss of function of ΔMER in DIOMs.
429 Our study provides new insights into the mechanisms underlying autophagy-
430 associated muscle remodeling. Transcriptional dynamics uncovered a sequence of events
431 involving muscle atrophy and hypertrophy, offering a valuable dataset for understanding the
432 process of muscle remodeling. In addition, we provided insights into the mechanism and
433 significance of BNIP3-mediated mitophagy *in vivo*. These findings are particularly important
434 given the evolutionary conservation of muscle remodeling mechanisms between *Drosophila* and
435 mammals (Piccirillo et al., 2014). Future studies should explore the broader implications of our
436 findings across various cellular, developmental, and organismal contexts.
437

438 **Materials and methods**

439 **Reagents and antibodies**

440 The following antibodies were used: Mouse monoclonal anti-ATP5A (1:300, ab14748, Abcam,
441 Cambridge, UK), Rat monoclonal anti-HA (1:1000; 11867423001, Roche, Basel, Switzerland),
442 Rabbit polyclonal anti-GFP (1:2000; 598, MBL, Nagoya, Japan), Rabbit polyclonal anti-
443 Fibrillarin (1:300; ab5821, Abcam, Cambridge, UK), anti-rabbit IgG Alexa Fluor 594 conjugate
444 (1:400; A11012, Thermo Fisher Scientific, Waltham, USA), anti-mouse IgG Alexa Fluor 488
445 conjugate (1:400; A11001, Thermo Fisher Scientific, Waltham, USA), anti-mouse IgG Alexa
446 Fluor 594 conjugate (1:400; A11005, Thermo Fisher Scientific, Waltham, USA), HRP-
447 conjugated AffiniPure Goat Anti-Rabbit IgG (1:10000; 111-035-144, Jackson
448 ImmunoResearch, West Grobe, USA), HRP-conjugated AffiniPure Donkey Anti-Rat IgG
449 (1:5000; 712-005-153, Jackson ImmunoResearch, West Grobe, USA), Bisbenzimide H33342
450 Fluorochrome Trihydrochloride DMSO Solution (1:10000; 04915-81, Nacalai Tesque, Kyoto,
451 Japan), Alexa Fluor 633 Phalloidin (1:200; A22284, Thermo Fisher Scientific, Waltham, USA),
452 and GFP-Trap Agarose (gta, Chromotek, Planegg-Martinsried, Germany).

453

454 ***Drosophila* strains**

455 Flies were reared under standard conditions at 25˚C unless otherwise stated. The w^{1118} strain
456 was used as a control for knockout strains. For muscle-targeted gene expression, Mef2-GAL4
457 was used. UAS-*LacZ* was used as a control for UAS transgenes. All genetic combinations were
458 generated by standard crosses. Detailed genotypes are described in Supplementary Table 1.
459 Genotypes of flies used in this study include the following: (1) y^{1} *w**; *P{*w^{+mC}*=GAL4-*
460 *Mef2.R}*3 (Bloomington *Drosophila* Stock Center, BL 27390; DMef2-GAL4), (2) w^{1118};
461 *P{*w^{+mC}*=UAS-lacZ.B}Bg4-1-2* (BL 1776; UAS-LacZ), (3) w^{*}; *P{*w^{+mC}*=UAS-Rheb.Pa}2* (BL
462 9688), (4) w^{1118}; *P{*w^{+mC}*=UAS-mito-HA-GFP.AP}2/CyO* (BL 8442; Mito-GFP), (5) w^{1118};
463 *P{*$y^{+t7.7}$ w^{+mC}*=UAS-mito-QC}attP16* (BL 91640, Mito-QC), (6) w^{1118}; *P{*w^{+mC}*=UAS-Dcr-*
464 *2.D}10* (BL 24651, *UAS-Dcr2*), (7) y^{*} w^{*}; *P{*w^{+mC}*=UAS-tdTomato.mito}2* (Kyoto DGGR
465 117016, tdTomato-Mito), (8) *w*; *UAS-IR-Atg18a*^{KK100064} (VDRC 105366; Atg18a RNAi), (9) *w*;
466 *UAS-IR-Stx17*^{KK100034} (VDRC 108825; Stx17 RNAi), (10) *w*; *UAS-IR-BNIP3*^{KK111246} (VDRC
467 107493; BNIP3 RNAi), (11) *w*; *UAS-IR-Pink1*^{KK101205} (VDRC 109614; Pink1 RNAi), (12) *w*;
468 *UAS-IR-Park*^{KK107919} (VDRC 104363; Park RNAi), (13) *w*; *UAS-IR-CG12511*^{KK109618} (VDRC

469 101785; CG12511 RNAi), (14) *w*; *UAS-IR-Zonda*^{KK107775} (VDRC 110620; Zonda RNAi), (15) y^1
470 sc^* v^1 sev^{21}; *P*{$y^{+t7.7}$ $v^{+t1.8}$=*TRiP.HMS01611*}*attP2*/*TM3, Sb*^{1} (TRiP, BL 36918; FIP200 RNAi),
471 (16) y^1 v^1; *P*{$y^{+t7.7}$ $v^{+t1.8}$=*TRiP.JF01937*}*attP2* (TRiP, BL 25896; Stx17 RNAi), (17) y^1 sc^* v^1
472 sev^{21}; *P*{$y^{+t7.7}$ $v^{+t1.8}$=*TRiP.GL00156*}*attP2* (TRiP, BL 35578; mTor RNAi), (18) *w*; *UAS-tub-*
473 *GAL80*^{ts} (from E. Kuranaga), (19) *w*; *UAS-mCD8:GFP*, (20) *w; DMef2-GAL4*, *UAS-Dcr2*
474 (Fujita et al., 2017), (21) *w*; *UAS-Dcr2*; *DMef2-GAL4*, *sqh-YFP:Mito*^{BL7194}/*TM6C Sb Tb*
475 (Murakawa et al., 2020). New genotypes generated during this study include the following: (22)
476 *w**;; *BNIP3 KO CRISPR{3xP3-RFP}/TM6B*, *Tb*^{1}, (23) w^{1118}, *Atg101 KO CRISPR{3xP3-*
477 *RFP}/FM7a* (24) w^{1118}; *UASt-GFP-BNIP3_full*^{attP40}, (25) w^{1118}; *UASt-GFP-BNIP3_ΔLIR*
478 (*W16A/L19A*)^{attP40}, (26) w^{1118}; *UASt-GFP-BNIP3_MER mutant* (*L49A*)^{attP40}, (27) w^{1118}; *UASt-*
479 *GFP-BNIP3_ΔMER* (*Δ*42-53)^{attP40} and (28) w^{1118}; *UASt-GFP-BNIP3_ ΔLIR+ΔMER*^{attP40}.
480

481 **DNA engineering**

482 Plasmid vectors were constructed using standard molecular biology techniques. The DNA
483 polymerase KOD One (TOYOBO, Osaka, Japan) and PrimeSTAR GXL Premix (Takara Bio,
484 Shiga, Japan) were used for PCR amplification. The DNA fragments were assembled using the
485 Gibson Assembly. Construction of the expression vectors of GFP-tagged BNIP3_full under
486 UAS control (pUASt-attB-GFP-BNIP3) was as follows: *Drosophila* BNIP3 CDS was amplified
487 from template RE48077 (DGRC Stock 9148; https://dgrc.bio.indiana.edu//stock/9148 ;
488 RRID:DGRC_9148) using the following primer sets: 5'-
489 ATGTCTACGACACCAAAATCGAG-3' and 5'-TCAGTCAATGACCACACGG-3'. This
490 fragment of BNIP3 CDS was ligated into the linearized pUAST-attB-GFP vector, which is
491 amplified with the following primer sets: 5'-
492 CGTGTGGTCATTGACTGAGCGGCCGCGGCTCGAGGGTACC-3' and 5'-
493 TTGGTGTCGTAGACATGGTGAAGGGGGCGGCCGCGGAG-3'. To generate plasmids with
494 mutations or deletions in the BNIP3 coding sequence (pUAST-attB-BNIP3_ΔLIR, pUAST-
495 attB-BNIP3_MER$^{mut\ (L49A)}$, and pUAST-attB-BNIP3_ΔMER), the plasmid pUAST-attB-GFP-
496 BNIP3_full was used as a template. For the construction of pUAST-attB-BNIP3_ΔLIR, these
497 primer sets: 5'- CTGCGATCGAAGCGAGCACAACAGCTGCGATG-3' and 5'-
498 CTCGCTTCGATCGCAGATTCGCCCAGCAAATC-3' were used to introduce the
499 W16A/L19A mutations. For the construction of pUAST-attB-BNIP3 MER$^{mut\ (L49A)}$, these primer

500 sets: 5'-AGACTTGCGCGCGAGGCCCAGCGCGAG-3' and 5'-
501 CTCGCGCGCAAGTCTCAGGTACTCCTC-3' were used to introduce the L49A mutation. For
502 the construction of pUAST-attB-BNIP3_ΔMER, these primer sets: 5'-
503 CAACAATCGCGAGTCGAACCAGTCG-3' and 5'-
504 GACTCGCGATTGTTGAATGGCAACGG-3' were used to delete G42 to Q53. To generate a
505 construct that harbors both ΔLIR and ΔMER (pUAST-attB-BNIP3_ΔLIR+ΔMER), the plasmid
506 pUAST-attB-GFP-BNIP3_ΔMER was used as a template. The same primer sets as pUAST-
507 attB-BNIP3_ ΔLIR construction were used for amplification. Each resultant linear DNA
508 fragment was ligated into a circular plasmid. Generation of the mammalian expression
509 constructs─pMRX-IRES-puro-GFP-BNIP3_full, pMRX-IRES-puro-GFP-BNIP3_ΔMER, and
510 pMRX-IRES-puro-3xHA-mCh-Atg18a─was performed by amplifying the corresponding
511 inserts from pUAST-attB-GFP-BNIP3_full, pUAST-attB-GFP-BNIP3_ΔMER, or LD38705
512 (DGRC Stock 2722; https://dgrc.bio.indiana.edu//stock/2722 ; RRID:DGRC_2722),
513 respectively. The amplified fragments were subsequently ligated into the linearized pMRX-
514 IRES-puro vector. All the resultant vectors were validated by DNA sequencing.
515
516 **Generation of mutant and transgenic flies**
517 To generate *Drosophila* mutants with a knockout of *BNIP3* (CG5059) or *Atg101* (CG7053), the
518 CRISPR/Cas9 system was used, following a modified method based on Kondo and Ueda
519 (Kondo and Ueda, 2013). Guide RNA (gRNA) sets for *BNIP3* KO and *Atg101* KO were
520 designed as follows: for *BNIP3* KO, upstream gRNA sequences, 5'-
521 CGTCAACACCAAAGATAACT[TGG]-3' and downstream gRNA sequences 5'-
522 CTTTCAGTCAATGACCACAC[GGG]-3'; for *Atg101 KO*, upstream gRNA sequences 5'-
523 GTCCACCTGACGACCCTCCA[TGG]-3' and downstream gRNA sequences 5'-
524 CTCGCAATGTGACGGGCTGT[CGG]-3'. Each gRNA was individually cloned into a plasmid
525 under the control of U6 promoter. A donor DNA cassette containing a 3x P3-RFP selection
526 marker, loxP sites, and two homology arms was cloned into the pUC57-Kan plasmid for DNA
527 repair. The gRNAs targeting *BNIP3* or *Atg101,* and the hs-Cas9 coding DNA plasmids, along
528 with the donor plasmid, were microinjected into embryos of the w^{1118} strain. F1 files were
529 screened by a selection marker of 3x P3-RFP and validated by genomic PCR and sequencing

530 (WellGenetics Inc.). To generate a series of UASt-GFP-BNIP3 transgenic flies, the vectors
531 described above were injected into embryos for phiC31-mediated insertion (WellGenetics Inc.).
532
533 **RNA-seq analysis of DIOMs**
534 For collecting DIOMs or their precursors, larvae or pupae were dissected and fixed with
535 methanol. Six DIOMs were isolated from each animal using forceps and a pipette under a
536 stereomicroscope (SZX16, EVIDENT, Tokyo, Japan). The collected muscle cells were lysed
537 with BLA buffer (ReliaPrep Tissue RNA Miniprep System, Promega) and stored at -80˚C.
538 Following sample preparation, the frozen samples were thawed, and total RNA was extracted
539 and eluted in RNase-free water according to the manufacturer's protocol (ReliaPrep Tissue
540 RNA Miniprep System, Promega). Subsequently, cDNA libraries were prepared using CEL-
541 Seq2, a single-cell RNA-seq protocol (Hashimshony et al., 2016). Briefly, reverse transcription
542 was performed using poly(T) primers with a T7 promoter to generate single-stranded DNA from
543 mRNA, which was then converted into double-stranded DNA through second-strand synthesis.
544 Amplified RNA was produced via in vitro transcription using the MEGAscript T7 kit (Thermo
545 Fisher Scientific, Waltham, MA) and subsequently reverse transcribed to construct the cDNA
546 library. Library sequencing was performed using the NovaSeq6000. Cell barcode and UMI in
547 Read1 were extracted by using UMI-tools with the following command "umi_tools extract -I
548 read1.fastq —read2-in=read2.fastq --bc-pattern=NNNNNNNNNNCCCCCCCC". Adaptor
549 sequence and low-quality sequence were removed, read lengths below 20bp were discarded by
550 using Trim Galore, and reads were mapped to the GRCm38 reference using HISAT2. Read
551 counts for each gene were obtained by featureCounts, and UMI duplications were removed. The
552 expression levels of genes in each sample were determined from the UMI counts after a
553 normalization process using the DESeq2 package in R. The R programming language was used
554 for each type of analysis, utilizing the pheatmap package for cluster analysis, the prcomp
555 package for principal component analysis (PCA), and the Mfuzz package for fuzzy c-means
556 clustering analysis (Kumar and Futschik, 2007).
557
558 **Quantification of rRNA in DIOMs**
559 Total RNA was extracted as described in the "RNA-seq analysis of DIOMs" section. The
560 quality and composition of the extracted RNA were assessed using the Agilent 2100

561 Bioanalyzer system with the RNA 6000 Pico Kit (Agilent, Santa Clara, USA). Ribosomal RNA
562 (rRNA) content in the DIOMs was quantified by measuring the peak areas corresponding to 18S
563 and 28S rRNA within the total RNA profile.
564
565 **Immunofluorescence staining**
566 Muscle preparations were performed as previously described (Ribeiro et al., 2011). 3IL or pupae
567 were pinned on a Sylgard-covered petri dish in dissection buffer (5 mM HEPES, 128 mM NaCl,
568 2 mM KCl, 4 mM $MgCl_2$, 36 mM sucrose, pH 7.2). The animals were pinned flat and fixed (4%
569 PFA, 50 mM EGTA, PBS) at room temp for 20 min. Then, the samples were unpinned and
570 blocked (0.3% bovine serum albumin, 0.6% Triton X100, PBS) at room temp for 5 min,
571 incubated with primary antibody overnight at room temperature, washed with PBS, and
572 incubated with Alexa Fluor 488 or 594-conjugated secondary antibody (Thermo Fisher
573 Scientific, Waltham, MA) for 2 h at room temperature. The immunostained samples were
574 washed and mounted in FluorSave reagent (Merck Millipore, Darmstadt, Germany).
575
576 **Confocal fluorescence microscopy**
577 To image live pupal DIOMs, staged pupae were removed from their pupal cases and mounted
578 between a slide glass and a cover glass following the protocol described by Zitserman and
579 Roegiers (Zitserman and Roegiers, 2011). Imaging was performed through the dorsal cuticle.
580 Both live and fixed samples were observed using a confocal microscope (FV3000, EVIDENT,
581 Tokyo, Japan) equipped with either a 60× silicone/1.30 NA UPlanSApo or a 4×/0.16 objective
582 lens (EVIDENT, Tokyo, Japan). FLUOVIEW (EVIDENT, Tokyo, Japan) was used for image
583 acquisition, and the exported images were processed and analyzed with ImageJ (NIH, Bethesda,
584 USA).
585
586 **Transmission electron microscopy**
587 Staged pupae (1 d or 4 d APF) were removed from pupal cases, pinned on a Sylgard-covered
588 petri dish, and dissected directly in fixative (2% paraformaldehyde, 2.5% glutaraldehyde, 150
589 mM, 5 mM calcium chloride, sodium cacodylate, pH 7.4). They were then fixed for 2 h at room
590 temperature followed by overnight at 4˚C. The dissected fillets were washed with 0.1 M
591 phosphate buffer pH 7.4, post-fixed in 1% OsO_4 buffered with 0.1 M phosphate buffer for 2 h,

592 dehydrated in a graded series of ethanol, and embedded flat in Epon 812 (TAAB, Aldermaston,
593 UK). Ultrathin sections (70 nm thick) were collected on copper grids covered with Formvar
594 (Nisshin EM, Tokyo, Japan), double-stained with uranyl acetate and lead citrate, and then
595 observed using a JEM-1400Flash transmission electron microscope (JEOL, Tokyo, Japan).
596
597 **Immunoblots and Immunoprecipitation**
598 For immunoblots, five larval fillets were collected for each sample. The samples were lysed
599 directly in 1.5x sample loading buffer [100 mM Tris-HCl (pH 6.8), 3% SDS, 15% glycerol, and
600 0.0015% Bromophenol Blue]. Equal amounts of proteins per sample were subjected to SDS-
601 PAGE and transferred to Immobilon-PSQ PVDF transfer membrane (Merck Millipore,
602 Darmstadt, Germany) with Trans-Blot Turbo Transfer System (Bio-Rad, Hercules, CA, USA).
603 The membranes were blocked with TBS-T buffer [10 mM Tris-HCl (pH 8.0), 150 mM NaCl,
604 0.1% Tween 20, PBS] containing 5% skim milk for 1 h, and were then incubated with primary
605 antibodies in Can Get Signal Solution 1 (TOYOBO, Osaka, Japan) overnight at 4˚C.
606 Membranes were washed three times with TBST, incubated with HRP-conjugated secondary
607 antibodies in the blocking buffer for 2 h at room temperature, and washed five times with
608 TBST. Immunoreactive bands were detected using Clarity Western ECL Substrate (Bio-Rad,
609 Hercules, CA, USA) and the ChemiDoc MP Imaging System (Bio-Rad, Hercules, CA, USA).
610 The images were processed using ImageJ.
611 For immunoprecipitation, HEK293 cells were transfected with plasmids using
612 jetPRIME transfection reagent (Polyplus-transfecton, Illkirch, France) according to the
613 manufacturer's instructions. The following plasmids were used: pMRX-IRES-puro (-), pMRX-
614 IRES-puro-GFP-BNIP3_full (Full), pMRX-IRES-puro-GFP-BNIP3_ΔMER (MERΔ), and
615 pMRX-IRES-puro-3xHA-mCh-Atg18a. After 24 h of transfection, cells were washed with PBS
616 and lysed in lysis buffer [20 mM HEPES (pH 7.4), 1 mM EDTA, 150 mM NaCl, 0.1% Triton
617 X-100, 10% glycerol, 1 mM PMSF, and protease inhibitor cocktail (Nacalai Tesque, Kyoto,
618 Japan)]. Cell lysates were centrifuged at 17,000 x g for 1 min at 4˚C, and the supernatants were
619 incubated with GFP-Trap agarose beads (Chromotek, Planegg-Martinsried, Germany) for 1.5 h
620 at 4˚C with gentle rotation. After incubation, beads were washed with Wash Buffer [20 mM
621 HEPES (pH 7.4), 150 mM NaCl, 0.1% Triton X-100, 10% glycerol] to remove non-specific

622 proteins. Bound proteins were eluted by boiling in 2x sample buffer for 5 min, and subsequent
623 steps were performed as described above for immunoblots.
624
625 **Structure prediction and visualization**
626 The amino acid sequences of *Drosophila* BNIP3 (Q9VPD6) and Atg18a (Q9VSF0) were
627 retrieved from the UniProt Knowledgebase (https://www.uniprot.org/uniprotkb/) and submitted
628 to the AlphaFold Server (https://alphafoldserver.com/) to predict the structure of their complex.
629 The PyMOL Molecular Graphics System (Version 2.5.4; Schrödinger, LLC) was then used to
630 analyze the resulting five predictions and visualize the top-ranked structure.
631
632 **Adult lifespan assay**
633 The Adult lifespan assay was performed according to a previously reported protocol (Linford et
634 al., 2013). Briefly, age-synchronized adult flies were collected, sorted by sex, and housed in
635 groups of 30 per vial. Flies were maintained at 25˚C under a 12 h light/12 h dark cycle and
636 transferred to fresh food vials every 2-3 days without anesthesia. Mortality was recorded at each
637 transfer, and statistical significance was determined using the log-rank test.
638
639 **Fly climbing assay**
640 The climbing assay was conducted according to the protocol previously published (Gevedon et
641 al., 2019). Adult flies were gently transferred without anesthesia into a vertical climbing
642 chamber composed of two connected vials, marked at 5 cm from the bottom. After a brief
643 recovery period, flies were tapped to the bottom of the chamber, and the number of flies that
644 climbed above the 5 cm mark within 10 seconds was recorded. The climbing success rate was
645 calculated as the percentage of flies that reached or surpassed the mark. Each group was tested
646 in five trials, with a rest period of several minutes between trials. The median success rate
647 across trials was used as the representative value for each group.
648
649 **Eclosion assay**
650 Late-stage pupae were collected and maintained at 25˚C. The eclosion process was recorded,
651 and the time from initial rupture of the pupal case to the complete emergence of the adult fly

652 was measured. For each group, 7 to 10 individuals were analyzed, and the average elapsed time
653 was calculated.
654
655 **Image analyses**
656 For cell volume measurement (Fig. 2E), the DIOMs expressing GFP were imaged at 1 μm
657 intervals. The muscle cell volume was calculated by multiplying the area of each XY slice by
658 the interval length and summing the results across all slices. To measure nucleolus and nucleus
659 volume (Fig. 2-figure supplement 2E and F), DIOMs stained for DNA (H33342) and Fibrillarin
660 were imaged at 0.5 μm intervals. DAPI- and anti-Fibrillarin-stained areas were extracted by
661 binarization using ImageJ. This process was repeated for the z-stacks, and the nucleolus and
662 nucleus volume were determined by multiplying the area of each slice by the interval length
663 between slices. For mitochondrial area measurement in TEM images (Fig. 4C), each
664 mitochondrion and the corresponding DIOM region were manually segmented, and the total
665 mitochondrial area and DIOM area per image were calculated for each image using ImageJ. The
666 total mitochondrial area was then normalized to the DIOM area. For each genotype, at least 9
667 images from multiple animals were analyzed. Quantification of the number of autophagosomes,
668 mitophagosomes, or mitochondria in TEM images was conducted as follows (Fig. 4D and E):
669 Double-membrane-bound structures containing undigested cytoplasmic contents
670 (autophagosomes), autophagosomes enclosing mitochondria (mitophagosomes), and unengulfed
671 mitochondria were manually counted. At least 17 images derived from multiple animals were
672 analyzed for each genotype. Mitochondrial area in DIOMs was quantified in Fig. 5D' 6A' and
673 6D'. Cellular regions containing F-actin were manually segmented, and tdTomato (Fig. 5D') or
674 GFP (Fig. 6A' and 6D') channel intensity within these segmented regions was measured. For
675 Fig. 5D' and 6A', image preprocessing steps, including filtering, background subtraction, and
676 intensity binarization, were applied to the tdTomato (Fig. 5D') or GFP (Fig. 6A') channel using
677 ImageJ to reduce noise. The area of each detected object was measured, and the total
678 mitochondrial area was defined as the sum of these object areas. Mitochondrial area values were
679 then normalized to the corresponding cellular region area. For Fig. 6D', GFP intensity
680 quantification was performed as follows: because GFP signals in the 3IL BWM images were
681 weaker than those at 4 d APF, the GFP channel intensity was uniformly enhanced across all
682 images at a constant scale. All images were preprocessed using filtering and background

683 subtraction. The mean GFP intensity within each segmented area was then measured and
684 normalized, with the mean GFP intensity of the control for each developmental stage set to 1.
685 For Fig. 5D', at least 46 DIOMs from 5 animals were analyzed per genotype. For Fig. 6A' and
686 6D', at least five DIOMs per fly were analyzed, with three biological replicates per genotype.
687 For the Mito-QC assay, a representative DIOM was imaged for each genotype and analyzed by
688 ImageJ (Fig. 6B). Image preprocessing included filtering and background subtraction for both
689 GFP and mCherry channels. Dot plots were then generated, and Pearson's correlation
690 coefficients for GFP and mCherry intensities were calculated using the *Coloc2* plugin in ImageJ
691 (Fig. 6B and B').
692
693 **Statistics**
694 Each experiment was performed with at least three different cohorts of unique flies analyzed.
695 One exception was for TEM analyses, performed on two parallel replicates with multiple
696 animals each. All experiments were performed in parallel with controls. Raw data files
697 corresponding to all quantified results are provided in Supplementary File 2. Error bars show
698 the standard deviation for bar charts. When more than two genotypes were used in an
699 experiment, Sidak's test, Kruskal-Wallis test, or Dunnett's T3 multiple comparisons test was
700 used (GraphPad, Prism9 version 9.5.1). Mann-Whitney tests were used to compare two
701 means. $P<0.05$ was regarded as statistically significant (*$P<0.05$, **$P<0.001$, ***$P<0.0001$,
702 and ****$P<0.00001$).
703

Acknowledgments

We are grateful to JH. Lee (Univ. of Michigan), T. Yoshimori (Osaka Univ.), E. Kuranaga (Kyoto Univ.), BDSC, VDRC, DGRC, and NIG-fly for reagents. We thank Y. Shimada and R. Niwa (Univ. of Tsukuba) for the helpful discussion. We thank the Biomaterials Analysis Division of the Institute of Science Tokyo, for the DNA sequencing. We are grateful to M. Landekic (McGill Univ.) for English editing. This work was supported in part by Grant-in-Aid for Transformative Research Areas (B) (grant number 21H05147, NF), Japan Science and Technology Agency (JST) PRESTO (grant number JPMJPR18H8, NF), AMED PRIME (grant number 24gm6410016h0001, NF), and MEXT Promotion of Development of a Joint Usage / Research System Project: Pan-Omics DDRIC, MRCI for High Depth Omics, CURE: JPMXP1323015486 for MIB, RIIT, and AMRC in Kyushu University.

Author contributions

NF conceived the project. HT, TM, TKanki, YO, and NF designed the experiments. HT, TM, KK, MK, TKaminishi, YS, KT, AH, and NF performed the experiments. HT, TM, and NF analyzed and interpreted data. YO contributed to the materials. NF took the lead in writing the manuscript. All authors provided critical feedback and helped shape the research and manuscript.

Competing financial interests

The authors declare no competing financial interests.

727 **References**

728 Abramson J, Adler J, Dunger J, Evans R, Green T, Pritzel A, Ronneberger O, Willmore L,
729 Ballard AJ, Bambrick J, Bodenstein SW, Evans DA, Hung CC, O'Neill M, Reiman D,
730 Tunyasuvunakool K, Wu Z, Žemgulytė A, Arvaniti E, Beattie C, Bertolli O, Bridgland A,
731 Cherepanov A, Congreve M, Cowen-Rivers AI, Cowie A, Figurnov M, Fuchs FB,
732 Gladman H, Jain R, Khan YA, Low CMR, Perlin K, Potapenko A, Savy P, Singh S,
733 Stecula A, Thillaisundaram A, Tong C, Yakneen S, Zhong ED, Zielinski M, Žídek A,
734 Bapst V, Kohli P, Jaderberg M, Hassabis D, Jumper JM. 2024. Accurate structure
735 prediction of biomolecular interactions with AlphaFold 3. *Nature* **630**:493–500.
736 doi:10.1038/s41586-024-07487-w
737 Adriaenssens E, Schaar S, Cook ASI, Stuke JFM, Sawa-Makarska J, Nguyen TN, Ren X,
738 Schuschnig M, Romanov J, Khuu G, Lazarou M, Hummer G, Hurley JH, Martens S. 2024.
739 Reconstitution of BNIP3/NIX-mediated autophagy reveals two pathways and hierarchical
740 flexibility of the initiation machinery. *bioRxiv* doi:10.1101/2024.08.28.609967
741 Bunker EN, Le Guerroué F, Wang C, Strub M, Werner A, Tjandra N, Youle RJ. 2023. Nix
742 interacts with WIPI2 to induce mitophagy . *EMBO J* **42**. doi:10.15252/embj.2023113491
743 Fujita N., Huang W, Lin T-H, Groulx J-F, Jean S, Nguyen J, Kuchitsu Y, Koyama-Honda I,
744 Mizushima N, Fukuda M, Kiger AA. 2017. Genetic screen in Drosophila muscle identifies
745 autophagy-mediated T-tubule remodeling and a Rab2 role in autophagy. *Elife* **6**.
746 doi:10.7554/eLife.23367
747 Gevedon O, Bolus H, Lye SH, Schmitz K, Fuentes-González J, Hatchell K, Bley L, Pienaar J,
748 Loewen C, Chtarbanova S. 2019. In Vivo Forward Genetic Screen to Identify Novel
749 Neuroprotective Genes in Drosophila melanogaster. *J Vis Exp*. doi:10.3791/59720
750 Guo T, Nan Z, Miao C, Jin X, Yang W, Wang Z, Tu Y, Bao H, Lyu J, Zheng H, Deng Q, Guo
751 P, YongmeiXi X, Yang X, Ge W. 2019. The autophagy-related gene Atg101 in Drosophila
752 regulates both neuron and midgut homeostasis. *Journal of Biological Chemistry*
753 **294**:5666–5676. doi:10.1074/jbc.RA118.006069
754 Hashimshony T, Senderovich N, Avital G, Klochendler A, de Leeuw Y, Anavy L, Gennert D,
755 Li S, Livak KJ, Rozenblatt-Rosen O, Dor Y, Regev A, Yanai I. 2016. CEL-Seq2: Sensitive
756 highly-multiplexed single-cell RNA-Seq. *Genome Biol* **17**. doi:10.1186/s13059-016-0938-
757 8
758 Hegedus K, Nagy P, Gáspári Z, Juhász G. 2014. The putative HORMA domain protein Atg101
759 dimerizes and is required for starvation-induced and selective autophagy in Drosophila.
760 *Biomed Res Int*. doi:10.1155/2014/470482
761 Johansen T, Lamark T. 2020. Selective Autophagy: ATG8 Family Proteins, LIR Motifs and
762 Cargo Receptors. *J Mol Biol*. doi:10.1016/j.jmb.2019.07.016

763 Kamiyama T, Niwa R. 2022. Transcriptional Regulators of Ecdysteroid Biosynthetic Enzymes
764 and Their Roles in Insect Development. *Front Physiol*. doi:10.3389/fphys.2022.823418
765 Kanki T, Wang K, Cao Y, Baba M, Klionsky DJ. 2009. Atg32 Is a Mitochondrial Protein that
766 Confers Selectivity during Mitophagy. *Dev Cell* **17**:98–109.
767 doi:10.1016/j.devcel.2009.06.014
768 Karsli-Uzunbas G, Guo JY, Price S, Teng X, Laddha S V., Khor S, Kalaany NY, Jacks T, Chan
769 CS, Rabinowitz JD, White E. 2014. Autophagy is required for glucose homeostasis and
770 lung tumor maintenance. *Cancer Discov* **4**:915–927. doi:10.1158/2159-8290.CD-14-0363
771 Kawaguchi K, Fujita N. 2024. Shaping transverse-tubules: central mechanisms that play a role
772 in the cytosol zoning for muscle contraction. *J Biochem*. doi:10.1093/jb/mvad083
773 Kondo S, Ueda R. 2013. Highly Improved gene targeting by germline-specific Cas9 expression
774 in Drosophila. *Genetics* **195**:715–721. doi:10.1534/genetics.113.156737
775 Kumar L, Futschik M. 2007. Software Mfuzz: A software package for soft clustering of
776 microarray data. *Bioinformation* **2**:5–7. doi:10.6026/97320630002005
777 Lamark T, Johansen T. 2021. Mechanisms of Selective Autophagy. *Annual Review of Cell and*
778 *Developmental Biology Annu Rev Cell Dev Biol* **37**:143–69. doi:10.1146/annurev-cellbio-
779 120219
780 Lee JJ, Sanchez-Martinez A, Zarate AM, Benincá C, Mayor U, Clague MJ, Whitworth AJ.
781 2018. Basal mitophagy is widespread in Drosophila but minimally affected by loss of
782 Pink1 or parkin. *Journal of Cell Biology* **217**:1613–1622. doi:10.1083/jcb.201801044
783 Li Y, Zheng W, Lu Y, Zheng Y, Pan L, Wu X, Yuan Y, Shen Z, Ma S, Zhang Xingxian, Wu J,
784 Chen Z, Zhang Xiangnan. 2022. BNIP3L/NIX-mediated mitophagy: molecular
785 mechanisms and implications for human disease. *Cell Death Dis*. doi:10.1038/s41419-
786 021-04469-y
787 Liang M, Hody C, Yammine V, Soin R, Sun Y, Lin X, Tian X, Meurs R, Perdrau C, Delacourt
788 N, Oumalis M, Andris F, Conrard L, Kruys V, Gueydan C. 2023. eIF4EHP promotes Ldh
789 mRNA translation in and fruit fly adaptation to hypoxia. *EMBO Rep* **24**.
790 doi:10.15252/embr.202256460
791 Lieber T, Jeedigunta SP, Palozzi JM, Lehmann R, Hurd TR. 2019. Mitochondrial fragmentation
792 drives selective removal of deleterious mtDNA in the germline. *Nature* **570**:380–384.
793 doi:10.1038/s41586-019-1213-4
794 Linford NJ, Bilgir C, Ro J, Pletcher SD. 2013. Measurement of lifespan in Drosophila
795 melanogaster. *Journal of Visualized Experiments*. doi:10.3791/50068
796 Lőrincz P, Juhász G. 2020. Autophagosome-Lysosome Fusion. *J Mol Biol*.
797 doi:10.1016/j.jmb.2019.10.028

798 Mao Q, Acharya A, Rodríguez-Delarosa A, Marchiano F, Dehapiot B, Tanoury Z Al, Rao J,
799 Díaz-Cuadros M, Mansur A, Wagner E, Chardes C, Gupta V, Lenne PF, Habermann BH,
800 Theodoly O, Pourquié O, Schnorrer F. 2022. Tension-driven multi-scale self-organisation
801 in human iPSC-derived muscle fibers. *Elife* **11**. doi:10.7554/eLife.76649
802 Masiero E, Agatea L, Mammucari C, Blaauw B, Loro E, Komatsu M, Metzger D, Reggiani C,
803 Schiaffino S, Sandri M. 2009. Autophagy Is Required to Maintain Muscle Mass. *Cell*
804 *Metab* **10**:507–515. doi:10.1016/j.cmet.2009.10.008
805 Mcguire SE, Mao Z, Davis R. 2004. Spatiotemporal gene expression targeting with TARGET
806 and gene-swich systems in Drosophila. *Sci STKE* doi:10.1126/stke.2202004pl6
807 Morishita H, Mizushima N. 2019. Annual Review of Cell and Developmental Biology Diverse
808 Cellular Roles of Autophagy Autophagosome: a double-membrane structure enclosing
809 cytoplasmic materials. *Annu Rev Cell Dev Biol* **35**:453–75. doi:10.1146/annurev-cellbio-
810 100818
811 Murakawa T, Kiger AA, Sakamaki Y, Fukuda M, Fujita N. 2020. An autophagy-dependent
812 tubular lysosomal network synchronizes degradative activity required for muscle
813 remodeling. *J Cell Sci* **133**. doi:10.1242/jcs.248336
814 Murakawa T, Nakamura T, Kawaguchi K, Murayama F, Zhao N, Stasevich TJ, Kimura H,
815 Fujita N. 2022. A Drosophila toolkit for HA-tagged proteins unveils a block in autophagy
816 flux in the last instar larval fat body. *Development (Cambridge)* **149**.
817 doi:10.1242/dev.200243
818 Nakatogawa H. 2020. Mechanisms governing autophagosome biogenesis. *Nat Rev Mol Cell*
819 *Biol*. doi:10.1038/s41580-020-0241-0
820 Narendra DP, Youle RJ. 2024. The role of PINK1–Parkin in mitochondrial quality control. *Nat*
821 *Cell Biol*. doi:10.1038/s41556-024-01513-9
822 Ney PA. 2015. Mitochondrial autophagy: Origins, significance, and role of BNIP3 and NIX.
823 *Biochim Biophys Acta Mol Cell Res*. doi:10.1016/j.bbamcr.2015.02.022
824 Niemi NM, Friedman JR. 2024. Coordinating BNIP3/NIX-mediated mitophagy in space and
825 time. *Biochem Soc Trans*. doi:10.1042/BST20221364
826 Noda NN, Mizushima N. 2016. Atg101: Not Just an Accessory Subunit in the Autophagy-
827 initiation Complex. *Cell Structure and Function*. doi:10.1247/csf.15013
828 Novak I, Kirkin V, McEwan DG, Zhang J, Wild P, Rozenknop A, Rogov V, Löhr F, Popovic D,
829 Occhipinti A, Reichert AS, Terzic J, Dötsch V, Ney PA, Dikic I. 2010. Nix is a selective
830 autophagy receptor for mitochondrial clearance. *EMBO Rep* **11**:45–51.
831 doi:10.1038/embor.2009.256

832 Okamoto K, Kondo-Okamoto N, Ohsumi Y. 2009. Mitochondria-Anchored Receptor Atg32
833 Mediates Degradation of Mitochondria via Selective Autophagy. *Dev Cell* **17**:87–97.
834 doi:10.1016/j.devcel.2009.06.013
835 Onishi M, Yamano K, Sato M, Matsuda N, Okamoto K. 2021. Molecular mechanisms and
836 physiological functions of mitophagy. *EMBO J* **40**. doi:10.15252/embj.2020104705
837 Palozzi JM, Jeedigunta SP, Minenkova A V., Monteiro VL, Thompson ZS, Lieber T, Hurd TR.
838 2022. Mitochondrial DNA quality control in the female germline requires a unique
839 programmed mitophagy. *Cell Metab* **34**:1809-1823.e6. doi:10.1016/j.cmet.2022.10.005
840 Piccirillo R, Demontis F, Perrimon N, Goldberg AL. 2014. Mechanisms of muscle growth and
841 atrophy in mammals and Drosophila. *Developmental Dynamics* **243**:201–215.
842 doi:10.1002/dvdy.24036
843 Quy PN, Kuma A, Pierres P, Mizushima N. 2013. Proteasome-dependent activation of
844 mammalian target of rapamycin complex 1 (mTORC1) is essential for autophagy
845 suppression and muscle remodeling following denervation. *Journal of Biological*
846 *Chemistry* **288**:1125–1134. doi:10.1074/jbc.M112.399949
847 Ribeiro I, Yuan L, Tanentzapf G, Dowling JJ, Kiger A. 2011. Phosphoinositide regulation of
848 integrin trafficking required for muscle attachment and maintenance. *PLoS Genet* **7**.
849 doi:10.1371/journal.pgen.1001295
850 Sandoval H, Thiagarajan P, Dasgupta SK, Schumacher A, Prchal JT, Chen M, Wang J. 2008.
851 Essential role for Nix in autophagic maturation of erythroid cells. *Nature* **454**:232–235.
852 doi:10.1038/nature07006
853 Sanger JW, Wang J, Fan Y, White J, Sanger JM. 2010. Assembly and dynamics of myofibrils. *J*
854 *Biomed Biotechnol*. doi:10.1155/2010/858606
855 Sartori R, Romanello V, Sandri M. 2021. Mechanisms of muscle atrophy and hypertrophy:
856 implications in health and disease. *Nat Commun*. doi:10.1038/s41467-020-20123-1
857 Saxton RA, Sabatini DM. 2017. mTOR Signaling in Growth, Metabolism, and Disease. *Cell*.
858 doi:10.1016/j.cell.2017.02.004
859 Schwarten M, Mohrlüder J, Ma P, Stoldt M, Thielmann Y, Stangler T, Hersch N, Hoffmann B,
860 Merkel R, Willbold D. 2009. Nix directly binds to GABARAP: A possible crosstalk
861 between apoptosis and autophagy. *Autophagy* **5**:690–698. doi:10.4161/auto.5.5.8494
862 Schweers RL, Zhang J, Randall MS, Loyd MR, Li W, Dorsey FC, Kundu M, Opferman JT,
863 Cleveland JL, Miller JL, Ney PA. 2007. NIX is required for programmed mitochondrial
864 clearance during reticulocyte maturation. *Proc. Natl. Acad. Sci. U.S.A.* **104**:19500-19505.
865 doi:10.1073/pnas.0708818104

866 Semenza GL. 2014. Oxygen sensing, hypoxia-inducible factors, and disease pathophysiology.
867 *Annual Review of Pathology: Mechanisms of Disease* **9**:47–71. doi:10.1146/annurev-
868 pathol-012513-104720
869 Strong LM, Chang C, Riley JF, Boecker CA, Flower TG, Buffalo CZ, Ren X, Stavoe AK,
870 Holzbaur EL, Hurley JH. 2021. Structural basis for membrane recruitment of ATG16L1
871 by WIPI2 in autophagy. *Elife* doi:10.7554/eLife
872 Vargas JNS, Hamasaki M, Kawabata T, Youle RJ, Yoshimori T. 2023. The mechanisms and
873 roles of selective autophagy in mammals. *Nat Rev Mol Cell Biol*. doi:10.1038/s41580-022-
874 00542-2
875 Wang X, Yu L, Wu AR. 2021. The effect of methanol fixation on single-cell RNA sequencing
876 data. *BMC Genomics* **22**. doi:10.1186/s12864-021-07744-6
877 Yamashita SI, Sugiura Y, Matsuoka Y, Maeda R, Inoue K, Furukawa K, Fukuda T, Chan DC,
878 Kanki T. 2024. Mitophagy mediated by BNIP3 and NIX protects against ferroptosis by
879 downregulating mitochondrial reactive oxygen species. *Cell Death Differ* **31**:651–661.
880 doi:10.1038/s41418-024-01280-y
881 Yoshii SR, Kuma A, Akashi T, Hara T, Yamamoto A, Kurikawa Y, Itakura E, Tsukamoto S,
882 Shitara H, Eishi Y, Mizushima N. 2016. Systemic Analysis of Atg5-Null Mice Rescued
883 from Neonatal Lethality by Transgenic ATG5 Expression in Neurons. *Dev Cell* **39**:116–
884 130. doi:10.1016/j.devcel.2016.09.001
885 Zhang J, Loyd MR, Randall MS, Waddell MB, Kriwacki RW, Ney PA. 2012. A short linear
886 motif in BNIP3L (NIX) mediates mitochondrial clearance in reticulocytes. *Autophagy*
887 **8**:1325–1332. doi:10.4161/auto.20764
888 Zhang S, Wu S, Yao R, Wei X, Ohlstein B, Guo Z. 2024. Eclosion muscles secrete ecdysteroids
889 to initiate asymmetric intestinal stem cell division in Drosophila. *Dev Cell* **59**:125-
890 140.e12. doi:10.1016/j.devcel.2023.11.016
891 Zhang X, Avellaneda J, Spletter ML, Lemke SB, Mangeol P, Habermann BH, Schnorrer F.
892 2024. Mechanoresponsive regulation of myogenesis by the force-sensing transcriptional
893 regulator Tono. *Current Biology*. doi:10.1016/j.cub.2024.07.079
894 Zitserman D, Roegiers F. 2011. Live-cell Imaging of Sensory Organ Precursor Cells in Intact
895 Drosophila Pupae. *J Vis Exp*. doi:10.3791/2706
896
897

898 **Figure legends**

899 **Figure 1. Time-course RNA-seq of the DIOM remodeling in wild-type *Drosophila***

900 (A) A timeline of DIOM remodeling. Samples were collected at five time points: third instar
901 larva (3IL) and 1 to 4 days after puparium formation (APF). (B) The scheme for sample
902 preparation of DIOMs. Red-colored rectangles indicate single DIOMs. (C) DESeq2 principal
903 component analysis (PCA) of all mRNA-seq libraries. The first four principal components are
904 shown. PC1-2, left; PC3-4, right. The dotted arrow in the PC1-2 plot represents the direction of
905 the transcription dynamics. (D) Heat map of fuzzy c-means cluster core expression profiles. All
906 genes were categorized into twelve clusters. (E) Factor loadings of each cluster to PC1-2 and
907 PC3-4. The circles show r = 0.8 (PC1-2) or r = 0.7 (PC3-4). (F) GO enrichment at each time
908 point during metamorphosis. The width of each line represents the expression level of the
909 clusters indicated.

910

911 **Figure 2. Transcriptional dynamics during DIOM remodeling is independent of**
912 **autophagy**

913 (A) A schematic of DIOM remodeling in wild-type and autophagy-deficient conditions.
914 Autophagy-dependent muscle atrophy starts at 12-14 h APF. (B) Genotypes and time points of
915 the comparative RNA-seq analysis (top) and a diagram of autophagosome formation (bottom).
916 *FIP200* or *Atg18a* RNAi blocks autophagosome formation. *Stx17* RNAi blocks the
917 autophagosome-lysosome fusion. (C) DESeq2 PCA of all mRNA-seq libraries. PC1-2, left;
918 PC3-4, right. A total of 20 samples were analyzed. (D and E) DIOM volume changes in control
919 or *FIP200* RNAi from 3IL to 4 d APF. DIOMs were labeled with GFP. Projected images of XY
920 and XZ planes are shown (D). (E) Relative DIOM cell volume for each genotype normalized to
921 3IL (set to 1). N=5 (Mann-Whitney test).

922

923 **Figure 3. Loss of BNIP3 results in accumulation of mitochondria in DIOMs**

924 (A) A schematic of 4 d APF DIOMs in wild-type, *FIP200* RNAi, or *Stx17* RNAi. (B) TEM
925 image of *Stx17* RNAi DIOM at 4 d APF. White arrowheads indicate autophagosome structures.
926 (C) TEM image of wild-type DIOM at 1 d APF. White arrows indicate mitophagosome
927 membrane structure. (D) The expression level of mitophagy regulators in DIOMs at 1 d APF. N
928 = 4. Normalized counts in RNA-seq are shown. (E) The expression level of *BNIP3* and *Fbxl4* in

929 DIOMs. N = 4. (F) A diagram illustrating the *BNIP3* knockout strategy, where all exons were
930 deleted using two gRNAs and replaced with a 3xP3-RFP marker. (G) Loss of BNIP3 phenotype
931 on mitochondria and myofibrils in DIOM at 4 d APF. XY (top) and XZ (bottom) planes were
932 shown.
933
934 **Figure 4. BNIP3 is required for mitophagosome formation**
935 (A and B) TEM images of DIOM transverse sections at 4 d APF in wild-type (A) or *BNIP3* KO
936 (B). Mitochondria are shown in green. (C) The percentages of mitochondrial area per unit area
937 in the indicated genotypes. wild-type, N = 9; *BNIP3* KO, N = 12 (Mann-Whitney test). (D and
938 E) TEM images of DIOM transverse sections at 4 d APF in *Stx17* RNAi (D and D') or a
939 combination of *Stx17* RNAi and *BNIP3* KO (E and E'). Mitophagosomes, pink; Mitochondria,
940 green; autophagosomes, blue. (F) The number of mitophagosomes and mitochondria per unit
941 area in the indicated genotypes. (G) The number of total autophagosomes, including
942 mitophagosomes, per unit area in the indicated genotypes. *Stx17* RNAi, N = 20; *Stx17* RNAi
943 and *BNIP3* KO, N = 17 (Mann-Whitney test) (F and G).
944
945 **Figure 5. The LIR and MER motifs are required for BNIP3-mediated mitochondrial**
946 **clearance**
947 (A) Schematics of *Drosophila* BNIP3 and its mutants. (B) The structure of the BNIP3-Atg18a
948 complex predicted by AlphaFold 3. Top, overview: Atg18a is depicted in white, featuring a β-
949 propeller structure consisting of seven blades, with blades 2 and 3 highlighted in green and pink,
950 respectively. For BNIP3, only residues 29–74 are shown in blue for clarity, with the α-helix
951 spanning residues 42–53 highlighted in yellow. Bottom, close-up view: Amino acids positioned
952 to form intramolecular contacts through their side chains are labeled and represented as sticks,
953 with potential hydrogen bonds shown as dashed lines. (C) GFP pulldown experiment between
954 GFP-BNIP3_full or MERΔ construct and HA-mCh-Atg18a in HEK293 cells. (D and D') BNIP3
955 rescue experiment in DIOMs at 4 d APF. The indicated GFP-tagged BNIP3 constructs and
956 tdTomato-Mito were co-expressed in *BNIP3* KO flies using the GAL4/UAS system (D). Single-
957 channel images corresponding to the merged panels are presented in Fig. 5-figure supplement
958 1B. The percentages of mitochondrial area in DIOMs for the indicated genotypes. Empty (-), N
959 = 46; Full, N = 55; ΔLIR, N = 52; MER^{mut}, N = 48; ΔMER, N = 54; ΔLIR+ ΔMER, N = 51

960 (Kruskal-Wallis test) (D'). (E) The amount of GFP-BNIP3 in *WT* and *Atg101* KO muscles. The
961 GFP-BNIP3 constructs were expressed by Mef2-GAL4 in *WT* or *Atg101* KO flies. Larval fillets
962 were lysed and subjected to western blotting for GFP. After immunoblotting, the membrane was
963 stained with CBB to assess total protein loading.
964
965 **Figure 6. BNIP3-mediated mitophagy eliminates larval muscle mitochondria during**
966 **muscle remodeling**
967 (A and A') Time course microscopy of Mito-GFP and F-actin in control or *BNIP3* KO during
968 DIOM remodeling (A). Single-channel images corresponding to the merged panels are
969 presented in Fig. 6-figure supplement 1A. Mitochondrial area relative to total cell area. For 3IL,
970 control, N = 18; *BNIP3* KO, N = 17. For 1 d APF, control, N = 20; *BNIP3* KO, N = 18 (Mann-
971 Whitney test) (A'). (B and B') Mitophagy assay using Mito-QC in DIOMs at 1 d APF. Pixel
972 intensity correlation profiles and Pearson's correlation coefficients (R values) are shown.
973 Control, N = 6; *BNIP3* KO, N = 5. *FIP*200 RNAi, N = 5 (Sidak's test). (C, D, and D') Scheme
974 of the use of GAL80 temperature-sensitive mutants ($GAL80^{ts}$). The animals were raised at 29°C
975 (Restrictive) to induce Mito-GFP expression until mid-3IL, then shifted to 18°C (Permissive) to
976 block expression (C). Mito-GFP and ATP5A immunostaining (total mitochondria) signals in
977 muscles at 3IL or 4 d APF (D). Mito-GFP intensities in muscles at each time point normalized
978 to control (set to 1). For 3IL, control, N = 16; *BNIP3* KO, N = 15. For 1 d APF, control, N = 15;
979 *BNIP3* KO, N = 15 (Mann-Whitney test) (D'). (E) A model of muscle remodeling with or
980 without BNIP3. Loss of BNIP3 leads to mitochondrial accumulation, which disrupts muscle
981 remodeling.
982
983

984 **Supplementary materials legends**

985

986 **Figure 1—figure supplement-1. RNA-seq of DIOM remodeling**

987 (A) Heatmap of comparisons for each sample based on correlation coefficients. (B) The
988 contribution ratios (bar) and cumulative contribution ratios (red-colored line) of PC1 to 10 are
989 shown. (C) Fuzzy c-means clustering categorized expressed genes in DIOMs into twelve
990 groups. (D) Violin plot showing the expression level of each cluster, with the number of genes
991 in each cluster indicated at the bottom.

992

993 **Figure 2—figure supplement-1. Expression levels of Atg18a, FIP200, and Stx17 during**
994 **DIOM remodeling**

995 (A) Heatmap of comparisons for each sample based on correlation coefficients. (B-D)
996 Expression levels of *Atg18a* (B), *FIP200* (C), and *Stx17* (D) in DIOMs under the indicated
997 conditions. N = 4.

998

999 **Figure 2—figure supplement-2. Effect of autophagy deficiency on transcription of**
1000 **ribosomal RNA and proteins**

1001 (A) Time-course analysis of the amount of rRNA during DIOM remodeling in the indicated
1002 genotypes. (B and C) Loss of autophagy on the number of nuclei in DIOMs at 3 d APF. Nuclei
1003 in DIOMs were stained with Hoechst (B). N = 6 (Sidak's test) (C). (D-F) Loss of autophagy on
1004 nucleolus volume in DIOMs at 3 d APF. DNA and fibrillarin were stained. XY and XZ planes
1005 are shown (D). The nucleolus (E) and nucleus (F) volumes were calculated from Z-series
1006 images. N = 12 (Dunnett's T3 multiple comparisons test). (G) A heatmap of the expression
1007 levels of RpLs (left) and RpSs (right) relative to control at each time point.

1008

1009 **Figure 3—figure supplement-1. Loss of BNIP3 on mitochondria and myofibrils in DIOMs**

1010 YFP-Mito and Phalloidin-Alexa633 (F-actin) staining in DIOMs at 4 d APF in the indicated
1011 genotypes.

1012

1013 **Figure 3—figure supplement-2. Loss of BNIP3 on adult fly lifespan and mobility**

1014 (A) Survival rates of wild-type and *BNIP3* KO adult males. *WT*, N = 298; *BNIP3* KO, N = 297.
1015 (Log-rank test). (B) Climbing ability of wild-type and *BNIP3* KO adult males at 1 and 4 weeks
1016 old. N = 6 (Mann-Whitney test). (C) Elapsed time to eclosion in wild-type males and *BNIP3*
1017 KO males. WT, N = 10; *BNIP3* KO, N = 7 (Mann-Whitney test).
1018
1019 **Figure 5—figure supplement-1. GFP-BNIP3 constructs localize to the outer mitochondrial**
1020 **membrane**
1021 (A) Localization of GFP-BNIP3 constructs and mitochondria matrix-targeted tdTomato
1022 (tdTomato-Mito) in 3IL BWMs. (B) BNIP3 rescue experiment in DIOMs at 4 d APF. The
1023 indicated GFP-tagged BNIP3 constructs and tdTomato-Mito were co-expressed in *BNIP3* KO
1024 flies using the GAL4/UAS system. Individual fluorescence channels are displayed separately.
1025
1026 **Figure 5—figure supplement-2. Effect of GFP-BNIP3 overexpression on mitophagy flux in**
1027 **3IL BWMs**
1028 GFP-BNIP3 or mitochondria matrix-targeted GFP (Mito-GFP) were overexpressed together
1029 with tdTomato-Mito in 3IL BWMs. No clear difference in tdTomato-Mito signal was observed
1030 between samples with or without GFP-BNIP3 overexpression.
1031
1032 **Figure 6—figure supplement-1. The impact of BNIP3 knockout on the shape of the DIOM**
1033 **during metamorphosis**
1034 (A) Time-course microscopy of mCD8-GFP in dorsal muscles imaged through the cuticle in
1035 control and BNIP3 KO animals from 3IL to 4 d APF. (B) Time-course microscopy of Mito-GFP
1036 and F-actin in control or *BNIP3* KO during DIOM remodeling. Individual fluorescence channels
1037 are displayed separately.
1038
1039 **Supplementary Table 1**
1040 Detailed Drosophila genotypes, developmental stages, and experimental temperatures are
1041 provided.
1042
1043 **Supplementary File 1**
1044 Normalized counts from time-course RNA-seq of DIOM remodeling during metamorphosis.

1045

1046 **Supplementary File 2**

1047 Raw data files corresponding to all quantified results presented in the manuscript.

1048

1049 **Data availability**

1050 RNA-seq data have been deposited in GEO under accession number GSE293359.

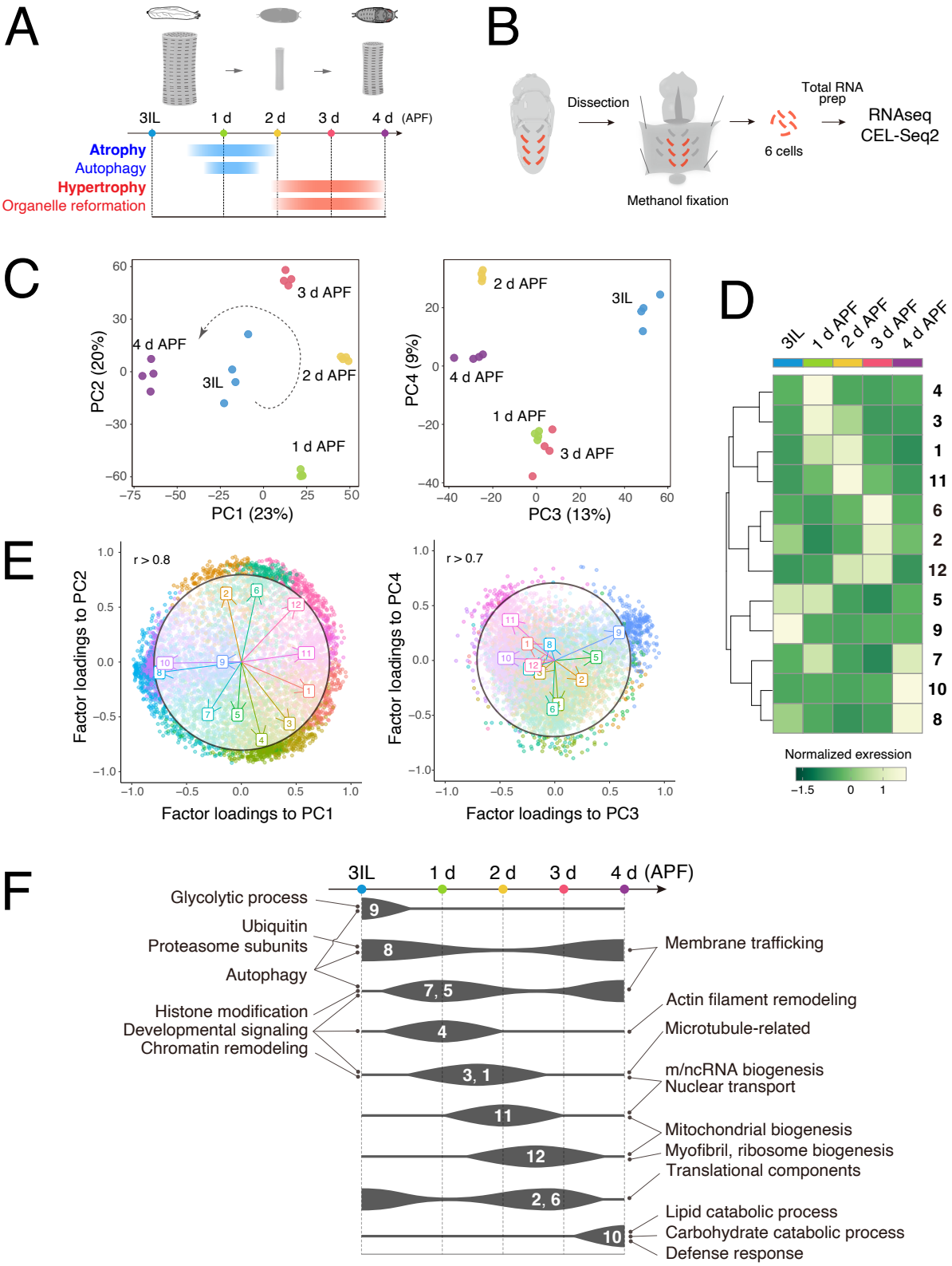
A
3IL
1 d
2 d
3 d
4 d (APF)
Atrophy
Autophagy
Hypertrophy
Organelle reformation
B
Dissection
Methanol fixation
6 cells
Total RNA prep
RNAseq
CEL-Seq2
C
PC2 (20%)
PC1 (23%)
3 d APF
4 d APF
3IL
2 d APF
1 d APF
PC4 (9%)
PC3 (13%)
2 d APF
3IL
4 d APF
1 d APF
3 d APF
D
3IL
1 d APF
2 d APF
3 d APF
4 d APF
Normalized exression
E
r > 0.8
Factor loadings to PC2
Factor loadings to PC1
r > 0.7
Factor loadings to PC4
Factor loadings to PC3
F
3IL
1 d
2 d
3 d
4 d (APF)
Glycolytic process
Ubiquitin
Proteasome subunits
Autophagy
Histone modification
Developmental signaling
Chromatin remodeling
Membrane trafficking
Actin filament remodeling
Microtubule-related
m/ncRNA biogenesis
Nuclear transport
Mitochondrial biogenesis
Myofibril, ribosome biogenesis
Translational components
Lipid catabolic process
Carbohydrate catabolic process
Defense response

Figure 1

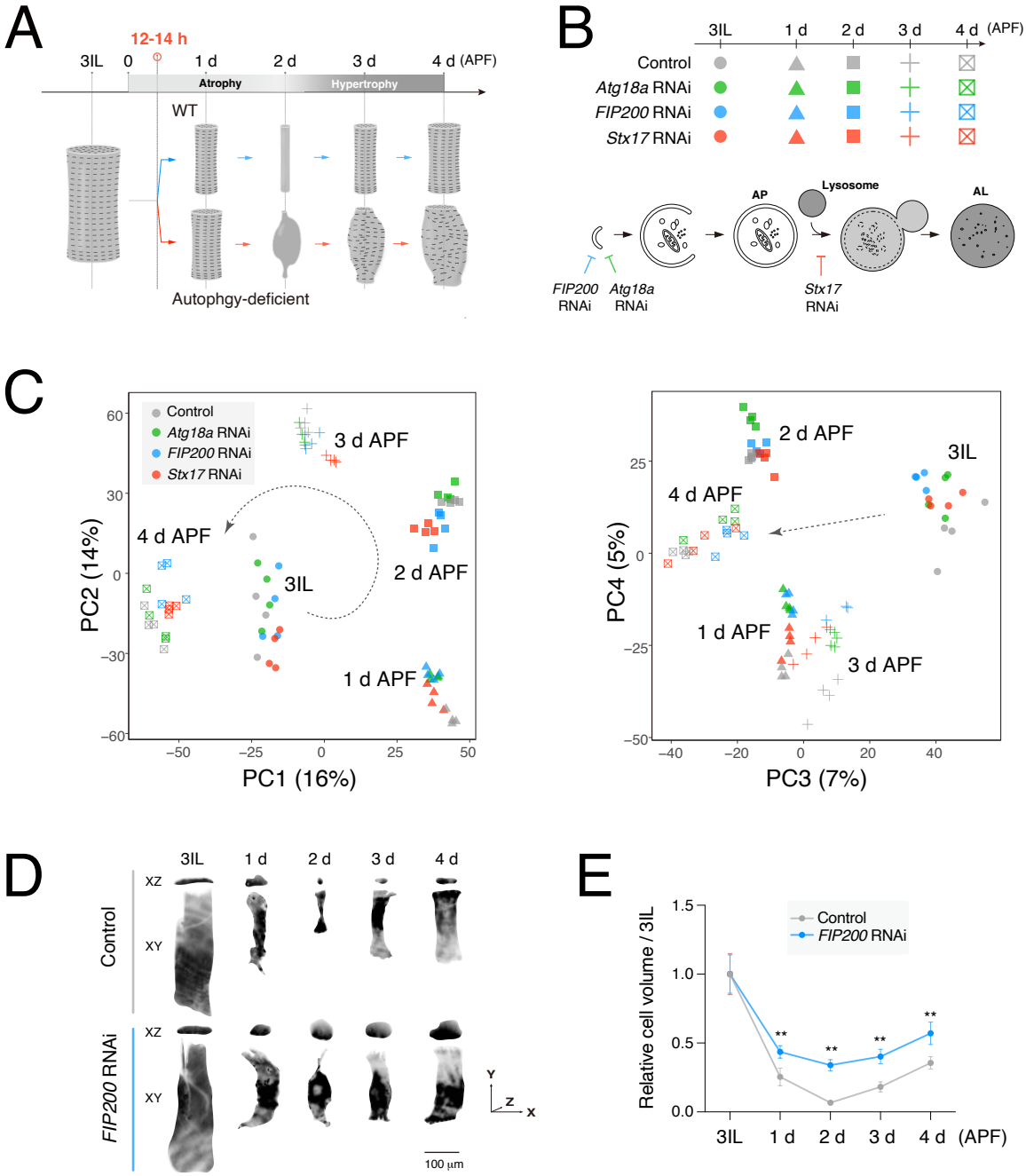
A
12-14 h
3IL
0
1 d
2 d
3 d
4 d (APF)
Atrophy
Hypertrophy
WT
Autophgy-deficient
B
3IL
1 d
2 d
3 d
4 d (APF)
Control
Atg18a RNAi
FIP200 RNAi
Stx17 RNAi
AP
Lysosome
AL
FIP200 RNAi
Atg18a RNAi
Stx17 RNAi
C
Control
Atg18a RNAi
FIP200 RNAi
Stx17 RNAi
3 d APF
4 d APF
3IL
2 d APF
1 d APF
PC2 (14%)
PC1 (16%)
2 d APF
3IL
4 d APF
1 d APF
3 d APF
PC4 (5%)
PC3 (7%)
D
3IL
1 d
2 d
3 d
4 d
Control
FIP200 RNAi
XZ
XY
Y
Z
X
100 µm
E
Control
FIP200 RNAi
Relative cell volume / 3IL
3IL
1 d
2 d
3 d
4 d
(APF)

Figure 2

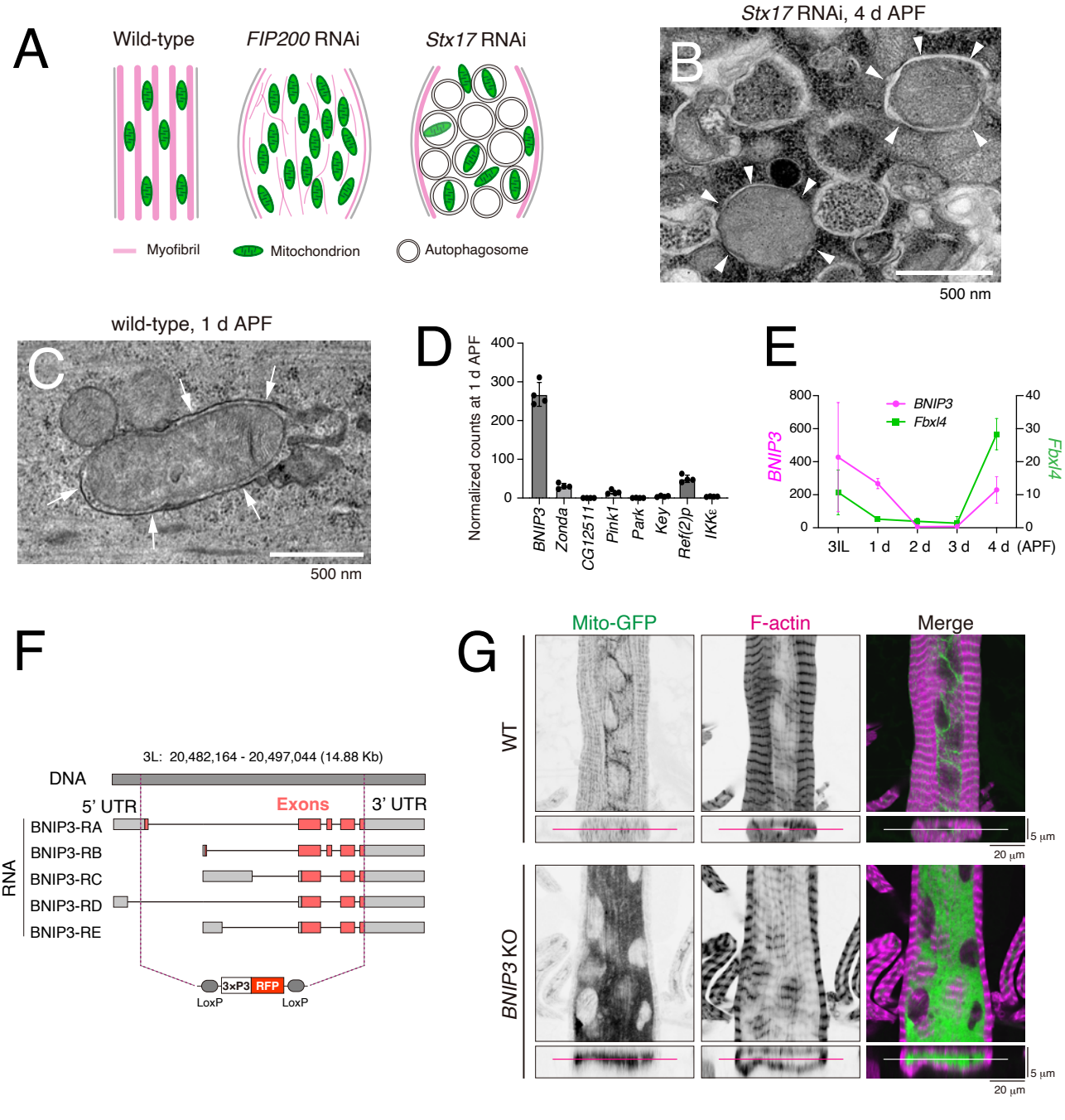
A
Wild-type
FIP200 RNAi
Stx17 RNAi
Myofibril
Mitochondrion
Autophagosome
Stx17 RNAi, 4 d APF
B
500 nm
wild-type, 1 d APF
C
500 nm
D
Normalized counts at 1 d APF
400
300
200
100
0
BNIP3
Zonda
CG12511
Pink1
Park
Key
Ref(2)p
IKKε
E
BNIP3
Fbxl4
800
600
400
200
0
40
30
20
10
0
3IL
1 d
2 d
3 d
4 d
(APF)
F
3L: 20,482,164 - 20,497,044 (14.88 Kb)
DNA
5' UTR
Exons
3' UTR
RNA
BNIP3-RA
BNIP3-RB
BNIP3-RC
BNIP3-RD
BNIP3-RE
3xP3
RFP
LoxP
LoxP
G
Mito-GFP
F-actin
Merge
WT
BNIP3 KO
5 µm
20 µm
5 µm
20 µm

Figure 3

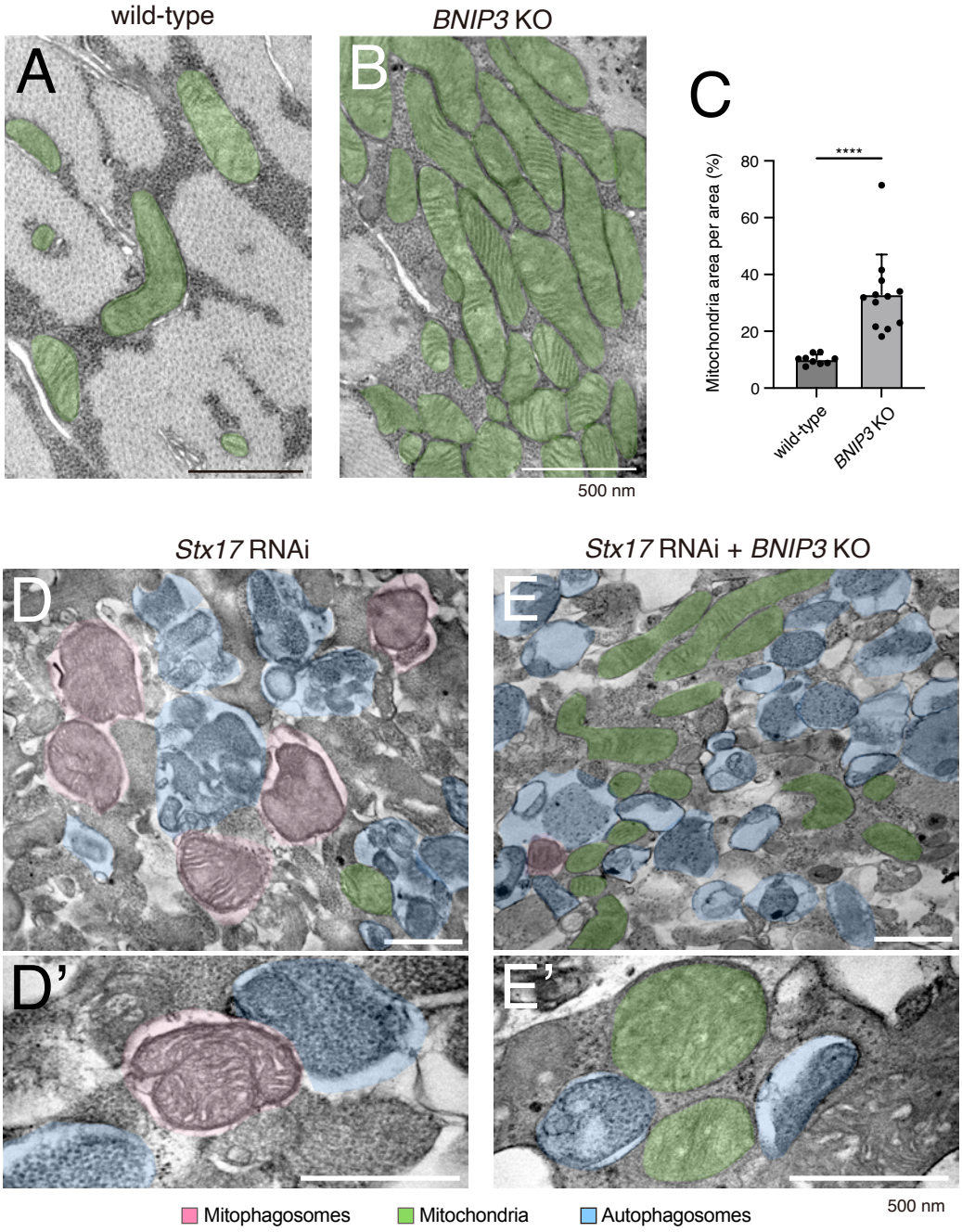
wild-type
BNIP3 KO
A
B
C
500 nm
Mitochondria area per area (%)
80
60
40
20
0
****
wild-type
BNIP3 KO
Stx17 RNAi
Stx17 RNAi + BNIP3 KO
D
E
D'
E'
500 nm
Mitophagosomes
Mitochondria
Autophagosomes

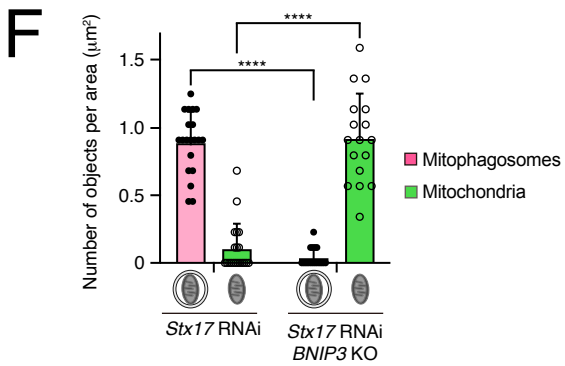
F
Number of objects per area (μm²)
1.5
1.0
0.5
0
****
****
Mitophagosomes
Mitochondria
Stx17 RNAi
Stx17 RNAi
BNIP3 KO

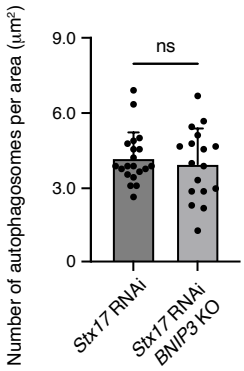
G
Number of autophagosomes per area (μm²)
9.0
6.0
3.0
0
ns
Stx17 RNAi
Stx17 RNAi
BNIP3 KO

Figure 4

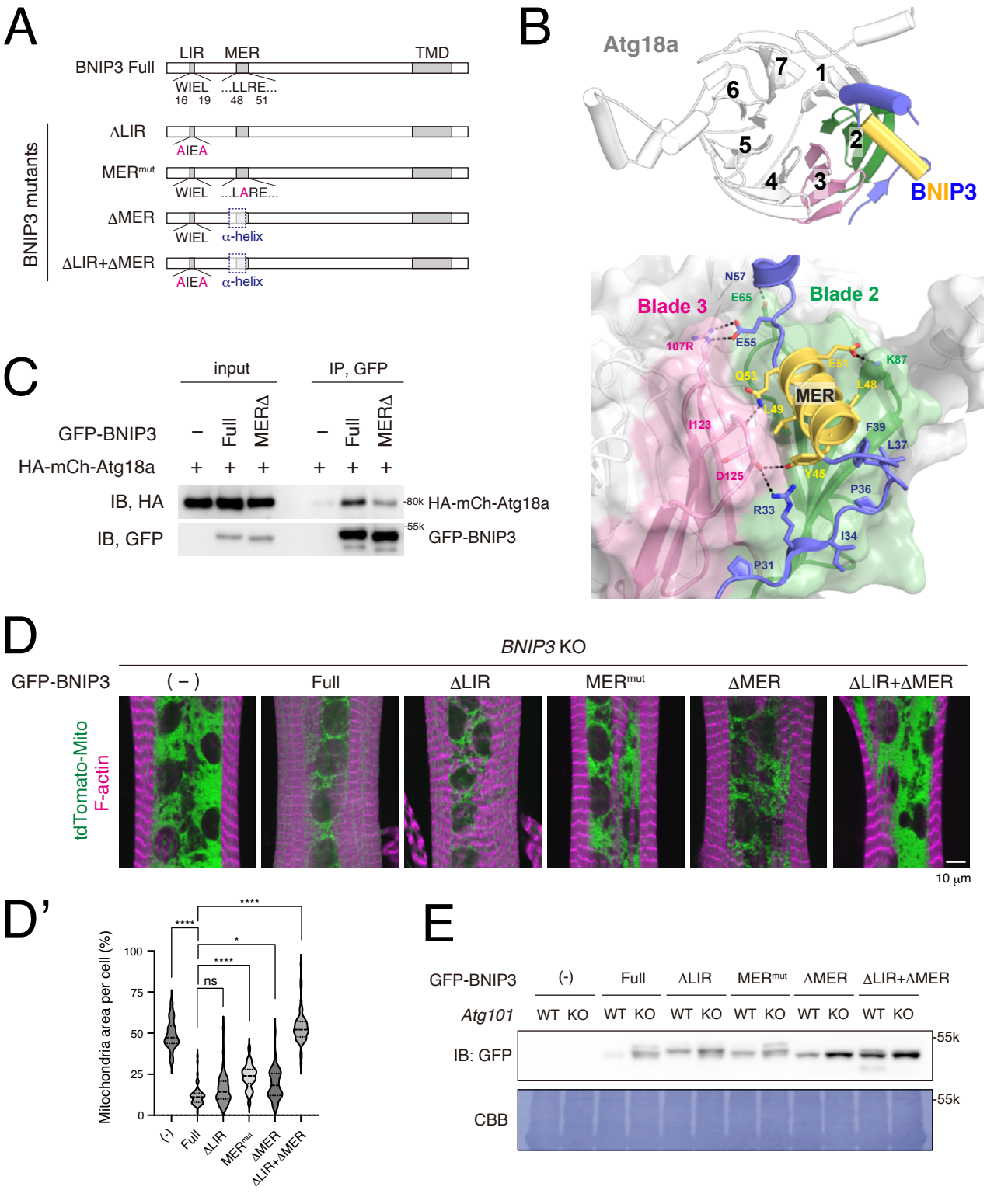
A
BNIP3 Full
LIR
MER
TMD
WIEL
...LLRE...
16 19
48 51
BNIP3 mutants
ΔLIR
AIEA
MERmut
WIEL
...LARE...
ΔMER
WIEL
α-helix
ΔLIR+ΔMER
AIEA
α-helix
B
Atg18a
BNIP3
C
input
IP, GFP
GFP-BNIP3
HA-mCh-Atg18a
IB, HA
IB, GFP
HA-mCh-Atg18a
GFP-BNIP3
D
BNIP3 KO
GFP-BNIP3
(–)
Full
ΔLIR
MERmut
ΔMER
ΔLIR+ΔMER
tdTomato-Mito
F-actin
10 μm
D'
Mitochondria area per cell (%)
E
GFP-BNIP3
Atg101
IB: GFP
CBB

Figure 5

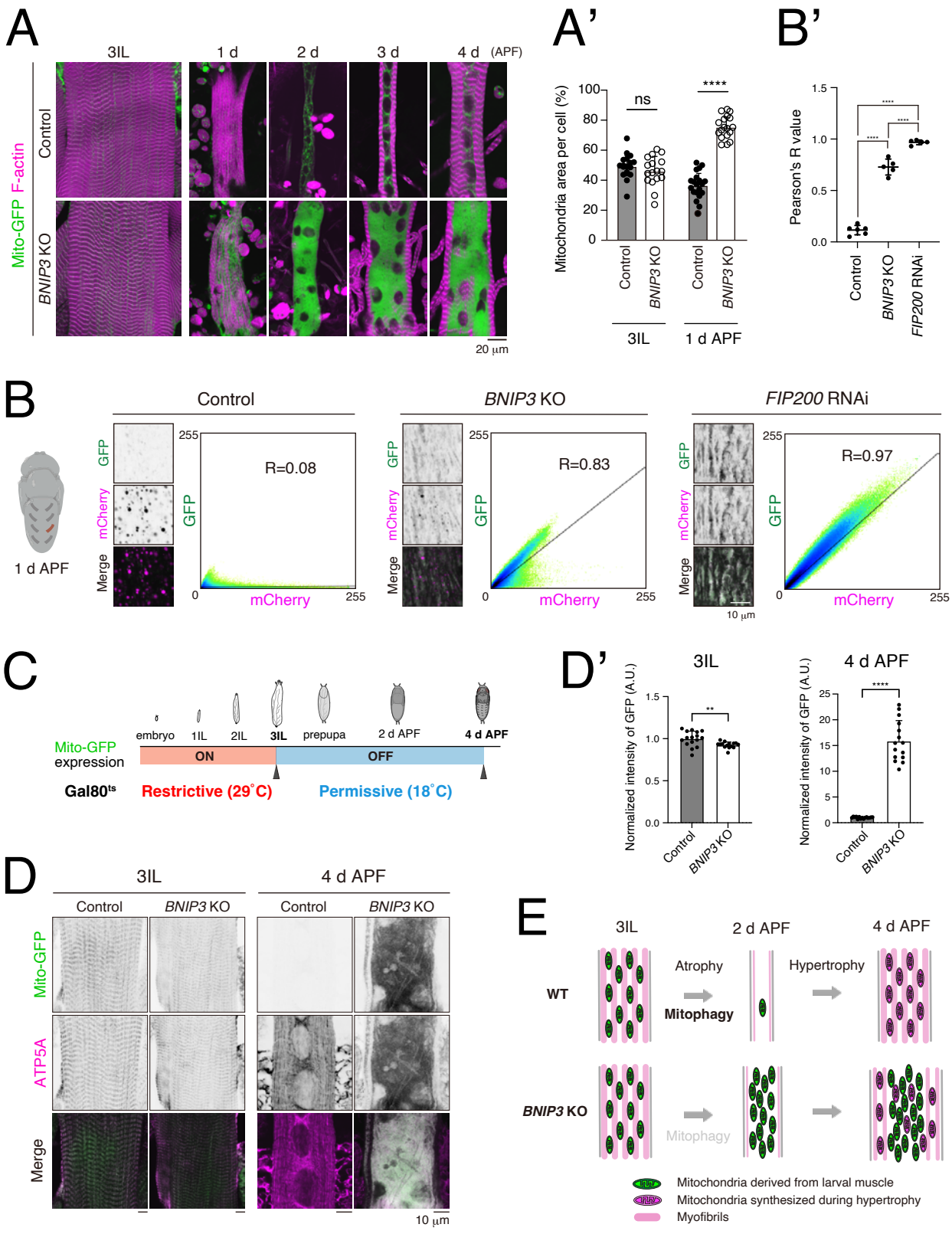
A
3IL
1 d
2 d
3 d
4 d (APF)
Mito-GFP F-actin
Control
BNIP3 KO
20 μm
A'
Mitochondria area per cell (%)
ns
****
Control
BNIP3 KO
3IL
1 d APF
B'
Pearson's R value
Control
BNIP3 KO
FIP200 RNAi
B
Control
BNIP3 KO
FIP200 RNAi
1 d APF
GFP
mCherry
Merge
R=0.08
R=0.83
R=0.97
255
0
10 μm
C
embryo
1IL
2IL
3IL
prepupa
2 d APF
4 d APF
Mito-GFP expression
ON
OFF
Gal80ts
Restrictive (29˚C)
Permissive (18˚C)
D'
3IL
4 d APF
Normalized intensity of GFP (A.U.)
Control
BNIP3 KO
D
3IL
4 d APF
Control
BNIP3 KO
Mito-GFP
ATP5A
Merge
10 μm
E
3IL
2 d APF
4 d APF
WT
Atrophy
Mitophagy
Hypertrophy
BNIP3 KO
Mitophagy
Mitochondria derived from larval muscle
Mitochondria synthesized during hypertrophy
Myofibrils

Figure 6